

# The role of grain boundaries in the initial oxidation behavior of austenitic stainless steel containing alloyed Cu at 700 °C for advanced thermal power plant applications



Ju-Heon Kim <sup>a,b,c</sup>, Byung Kyu Kim <sup>a,b</sup>, Dong-Ik Kim <sup>a,\*</sup>, Pyuck-Pa Choi <sup>c</sup>, Dierk Raabe <sup>c</sup>, Kyung-Woo Yi <sup>b,\*</sup>

<sup>a</sup> High Temperature Energy Materials Research Center, Korea Institute of Science and Technology, Hwarangno 14-gil 5, Seongbuk-gu, Seoul 136-791, Republic of Korea

<sup>b</sup> Department of Materials Science and Engineering, Seoul National University, 1 Gwanak-ro, Gwanak-gu, Seoul 151-744, Republic of Korea

<sup>c</sup> Department of Microstructure Physics and Alloy Design, Max-Planck Institut für Eisenforschung, Max-Planck Str. 1, 40237 Düsseldorf, Germany

## ARTICLE INFO

### Article history:

Received 29 November 2014

Accepted 7 March 2015

Available online 10 April 2015

### Keywords:

A. Stainless steel

B. TEM

B. SEM

C. Oxidation

## ABSTRACT

The role of grain boundaries during the early stages of oxidation in austenitic stainless steels containing alloyed Cu was investigated using APT, TEM, EBSD, EPMA, and XRD. The oxidation experiments were performed at 700 °C in air with 20% water vapor. Within 4 μm from the grain boundaries, the oxide layer exhibits a dual-layer structure consisting of a thin Fe-rich spinel oxide on a protective Cr<sub>2</sub>O<sub>3</sub> oxide. Away from the grain boundaries, non-protective spinel oxide layers are formed as the outer and inner oxide layers. A critical grain size that prevents the formation of fast-growing spinel oxides is discussed.

© 2015 Elsevier Ltd. All rights reserved.

## 1. Introduction

Despite enormous research efforts into renewable energy technologies, conventional thermal power plants are still by far the most important power generation source worldwide; thermal power plants are expected to maintain this position for at least several decades [1]. All power generation sources based on fossil fuel burning inevitably produce CO<sub>2</sub>, one of the major causes of global warming. Considering the contribution to the total CO<sub>2</sub> emission, improving fossil fuel-based energy conversion efficiency to 60% by increasing the reaction temperature is the most efficient way to reduce total CO<sub>2</sub> emissions by up to 30% [2,3].

Ultra supercritical (USC) coal-fired thermal power plants are operated at a steam pressure of ≥24.1 MPa and a steam temperature of ≥593 °C [4,5] in the boiler tube main line, such as in the superheater and reheater. These conditions require new boiler tube materials that can resist these extreme temperature and pressure conditions. In this context, there are two main requirements for boiler tube materials: creep strength and oxidation resistance. Austenitic stainless steels are considered candidate alloys for boiler tubes due to their higher strength at these operating conditions compared with the previously used ferritic stainless steels [3,5].

Austenitic stainless steels containing alloyed Cu were developed in the 1990s based on conventional 304 stainless steels, by the addition of Cu to form stable copper precipitates [4,6,7]. Similar lattice parameters and a small interfacial energy between the copper precipitates and austenitic matrix retard precipitate growth at high temperature [8], enabling the material to maintain its high creep strength [9,10].

Steam-side oxidation of the boiler tube is one of the main mechanisms of power plant failure aside from creep rupture, where the failure occurs due to poor adhesion of the oxide. In particular, Fe-rich oxides are considered poorly adhesive and non-protective, rendering the alloy susceptible to cracks and spallation during operation. The lifetime of boiler tube materials depends strongly on their resistance to oxidation.

Oxidation of austenitic stainless steel has already been studied by several authors as a function of the alloy composition [11], surface treatment and preparation [12–20], temperature [11,12,18,19,21–23], flow rate [24–26], water vapor [24,25,82] and oxygen partial pressure [12,24,27]. These works show that such steels can form a stable, dense, continuous, adherent and protective oxide layer consisting of various oxides, such as Cr<sub>2</sub>O<sub>3</sub>, SiO<sub>2</sub> or Al<sub>2</sub>O<sub>3</sub>, above 700 °C [28–30]. The initial stages of oxidation of chromium containing alloys, such as the AISI 304 stainless steels, involve the formation of a protective oxide layer, typically Cr<sub>2</sub>O<sub>3</sub>, followed by the formation of a spinel-type oxide [12,31–33]. The protective Cr<sub>2</sub>O<sub>3</sub> oxide layers on stainless steel considerably reduce the

\* Corresponding authors. Tel.: +82 2 958 5432; fax: +82 2 958 5379 (D.-I. Kim), Tel.: +82 2 880 8318; fax: +82 2 883 8197 (K.-W. Yi).

E-mail addresses: [dongikkim@kist.re.kr](mailto:dongikkim@kist.re.kr), [dongikkim@gmail.com](mailto:dongikkim@gmail.com) (D.-I. Kim), [yikw@snu.ac.kr](mailto:yikw@snu.ac.kr) (K.-W. Yi).

oxidation rate in highly aggressive environments [34,35], but their formation requires a Cr concentration of >18 wt.% to prevent the oxidation of stainless steels [36–38]. However, the resistance to high temperature oxidation of stainless steels deteriorates if they are exposed to the air containing water vapor. Water vapor is attributed to the water–vapor-assisted evaporation of chromium from the oxide in the form of a chromium oxide hydroxide, which makes difficult to maintain protective Cr<sub>2</sub>O<sub>3</sub> oxide layers [24,25,82]. The grain size of the substrate also plays an important role in the oxidation behavior because it affects the amount of Cr supplied to the surface due to the difference in Cr diffusivity along the grain boundaries and through the bulk grains [12,18,29,35,39–42].

To characterize the oxide layers, various analytical techniques, such as X-ray photoemission spectroscopy (XPS) [26,42], Auger electron spectroscopy (AES) [21,24–27], secondary ion mass spectroscopy (SIMS) [19,26], transmission electron microscopy (TEM) [13,43,44] and atom probe tomography (APT) [44–46], have been applied. Each of these methods has specific drawbacks when acquiring quantitative data, but they can provide useful information about thin surface oxide layers when used together. In this study, we investigated the early stage oxidation behavior of an austenitic stainless steel containing alloyed Cu. Complementary APT, TEM, electron backscattered diffraction (EBSD), electron probe microanalyzer (EPMA) and X-ray diffraction (XRD) analyses were introduced to elucidate compositional and structural changes upon oxidation at 700 °C. An intensive investigation to reveal the role of grain boundaries in the initial stages of oxidation was performed. The critical grain size to form a protective oxide is discussed based on the variations in the Cr contents as a function of the distance from the grain boundary.

## 2. Experimental

### 2.1. Alloy processing

An austenitic stainless steel containing 18% Cr, 9% Ni, 0.1% C, and 3% Cu (in wt.%) was produced via vacuum induction melting. The nominal composition of the alloy is given in Table 1. The chemical analysis was performed using inductively coupled plasma mass spectrometry (ICPMS). The ingot was solution treated for 24 h at 1200 °C, forged at 1200 °C and cooled in air. Subsequently, the sample was hot rolled at 1150 °C to 75% reduction in thickness. Three different thermo-mechanical processes, various combinations of cold rolling and annealing heat treatments, were applied to obtain different average grain sizes [41]. The first sample was only solution treated, annealed at 1150 °C for 30 min and then water quenched; this sample is referred to as the 'large grain' sample (average grain size was 27 μm). The second sample was multi-step deformed and annealed, cold rolled with a 5% reduction per pass and annealed at 1000 °C for 30 min between subsequent passes up to an 80% total reduction; this sample is referred to as the 'medium grain' sample (average grain size was 17 μm). The last sample was one step deformed and annealed, 80% cold rolled by one pass and annealed at 1000 °C for 1 min; this sample is referred to as 'small grain' sample (average grain size was 8 μm). For the oxidation studies, rectangular samples with lengths of 10 mm, widths of 7 mm and thicknesses of 2 mm were cut from the centers of the bulk materials.

**Table 1**  
Bulk chemical composition of the Cu-added austenitic stainless steel (in wt.% and at.%).

	Fe	Cr	Ni	Mn	Cu	Nb	Si	C	N
wt.%	Bal.	18.20	9.28	0.78	2.96	0.41	0.20	0.11	0.11
at.%	Bal.	19.29	8.71	0.78	2.57	0.24	0.39	0.51	0.43

### 2.2. High-temperature oxidation experiments

Before the oxidation test, the surfaces and edges of the samples were mechanically polished with SiC paper of up to 1200 grit and then electropolished at –30 °C using an electropolisher (LectroPol-5, Struers, Denmark) at 18 V for 30 s to obtain a deformation-free surface for EBSD analysis. For the electrolyte, a solution containing 590 ml of methanol, 350 ml of methyl propanol and 60 ml of perchloric acid was used. Then the samples were ultrasonically cleaned in an acetone–ethanol mixture and finally dried. After the EBSD analysis, the oxidation tests were performed at 700 °C in air with 20% water vapor for 30 min to 12 h. This temperature value is as high as the proposed advanced ultra super critical (A-USC) thermal power plant operation condition and has been selected to simulate a harsh environment and accelerate the degradation of the materials. Fig. 1 shows the set-up of the oxidation test under water vapor-containing conditions. This setup consists of three main parts. An air–H<sub>2</sub>O mixture was produced by passing synthesized air (99.9%) at a stable flow rate of 0.6 L/min (air supplement) through deionized water maintained at 75 °C (water vapor controller) and a tubular furnace fitted with a 70 mm diameter quartz tube (oxidation furnace). The horizontal furnace temperature was maintained ±2 °C as measured using a calibrated K-type thermocouple. The furnace was set to the desired temperature before inserting the samples. The samples were placed in a high-purity alumina (Al<sub>2</sub>O<sub>3</sub>) crucible. After 1, 2, 6, 12, and 28 h of oxidation, the samples were removed from the furnace and weighed using a high-sensitivity microbalance (MSE3.6P, Sartorius Weighing Technology GmbH, Germany: accuracy of ±10<sup>–5</sup> g after room temperature cooling).

### 2.3. Oxide layer analysis

#### 2.3.1. Atom probe tomography and transmission electron microscopy

APT analyses of the oxides formed during the initial stages were conducted using a local electrode atom probe (LEAP 3000X HR, Imago Scientific Instrument, Cameca, Madison, USA). The cross-sectional morphology and diffraction patterns of the oxide layers were observed using TEM (Tecnai F20, FEI, USA). APT and TEM samples were prepared from identical grain and grain boundaries, where the locations analyzed with APT and TEM were separated by ~4 μm. The site-specific sample preparation is illustrated in Fig. 2. A Ni layer was sputter-deposited to protect the brittle oxide layer on the substrate. Both APT and TEM samples were prepared using a dual-beam focused ion beam (FIB) device (Helios Nanolab 600i, FEI, USA) and the lift-out method. The TEM lamella was attached to a Cu grid and thinned using FIB milling to a thickness of ~50 nm. Needle-shaped APT samples were prepared via a lift-out procedure similar to the TEM sample preparation, mounting on an array of Si microtips and annular FIB milling [47–49]. To reduce the Ga<sup>+</sup> ion beam damage, both the APT and TEM samples were FIB milled using an ion energy of 5 kV in the final preparation steps. The applied acceleration voltage for TEM analysis was 200 kV. Based on the results obtained in previous studies [44,46], APT analysis was performed in laser mode, applying laser pulses with a wavelength of 532 nm, a 200 kHz pulse frequency and a 0.6 nJ pulse energy with a specimen temperature of ~60 K. The APT data reconstruction and analysis were performed using the IVAS 3.6.6 software from CAMECA (France).

#### 2.3.2. Scanning electron microscopy, electron backscattered diffraction and electron probe microanalysis

The oxide layers were also analyzed using SEM (S-4300SE, Hitachi, Japan) in combination with an EBSD system (e<sup>–</sup> Flash<sup>HR</sup>, Bruker, Germany). The EBSD experiments were performed using a 20 kV accelerating voltage and a 4 nA probe current. To

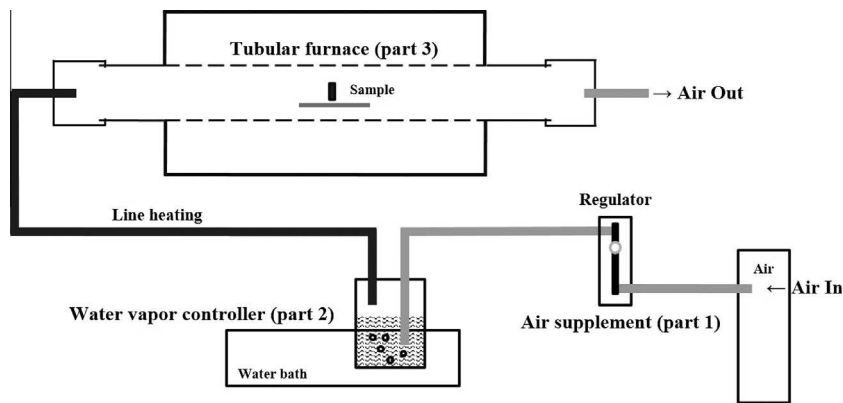


Fig. 1. Experimental setup for oxidation testing in a flowing atmosphere containing H<sub>2</sub>O vapor.

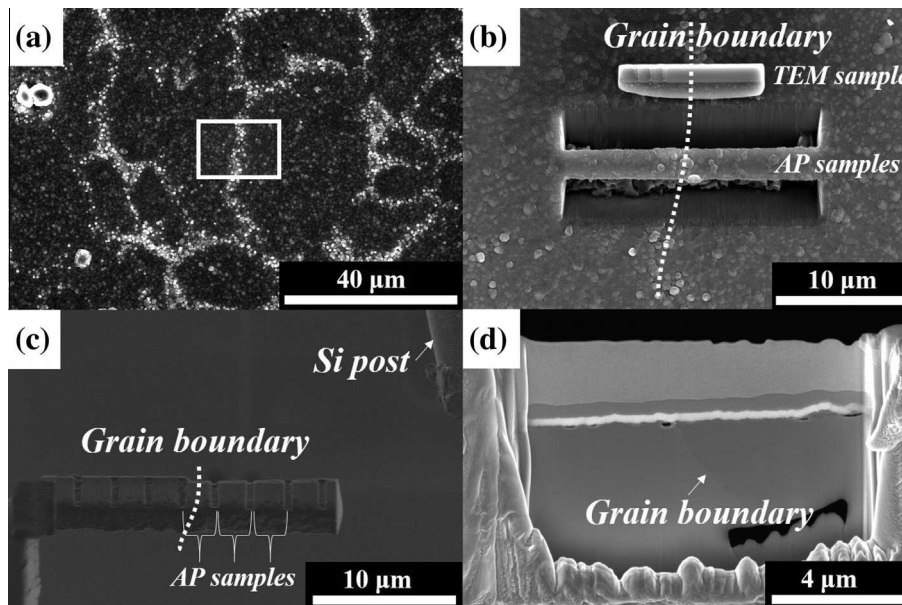


Fig. 2. Site-specific APT/TEM sample preparation method to jointly map the structure and composition of the selected regions, e.g., at grain boundaries in the medium grain sample after 30 min of oxidation at 700 °C in air with 20% water vapor. (a) Ni-coated surface to protect the oxide layer and selected region of interest (white box) containing a random grain boundary. (b) Pt electron-beam and ion-beam deposition for TEM sample preparation and 1st/2nd mill cut for APT sample preparation. (c) The APT samples with positions away from the actual grain boundary were lifted out using a micromanipulator. (d) The thin TEM lamella sample containing the grain boundary.

quantitatively analyze the average grain size and number fraction of coincidence site lattice (CSL) grain boundaries, ideally more than 100 grains per map were analyzed using EBSD with a step size of 0.1–0.5 μm. The grain size distribution and number fraction of CSL grain boundaries were analyzed using the Esprit 1.9.4 software from Bruker (Germany). The grains were reconstructed using a 5° misorientation angle criterion and by both considering and neglecting the Σ3 twin boundaries. Additionally, the surface oxide composition and elemental distributions were determined using EPMA (JXA-8500F, JEOL, Japan).

### 2.3.3. X-ray diffraction

Phase analyses of the oxide scale were performed using XRD (D8 advance, Bruker, Germany, Cu K $\alpha$  radiation:  $\lambda = 0.154$  nm). The XRD data were obtained by point scanning in the  $2\theta$  angular range from 15° to 80° with a step size of 0.02° ( $2\theta$ ) and a scan time of 2 s per step at room temperature. The diffraction patterns were indexed using the X'Pert HighScore Plus software from PANalytical (Nederland) with the JCPDS database.

## 3. Results

### 3.1. Oxidation behavior up to 30 min

#### 3.1.1. Selective oxidation behavior of austenitic stainless steel containing alloyed Cu

In ferritic stainless steels, selective oxidation that depended on the grain orientation and grain boundary characteristics was reported for dry air oxidation [50,51], whereas in austenitic stainless steels, selective oxidation that depended on the grain size was reported for humid air oxidation [41]. Back scattered electron (BSE) images (composition contrast) and EBSD band contrast maps obtained from identical regions of the medium grain sample are shown in Fig. 3 before and after 30 min of oxidation at 700 °C in air with 20% water vapor. As shown in Fig. 3(a), delayed oxidation behavior was observed within a certain distance from the grain boundaries. The light gray regions mark a grain boundary, whereas the dark gray regions correspond to the grain interior. The identified grain boundaries were random, high-angle grain boundaries

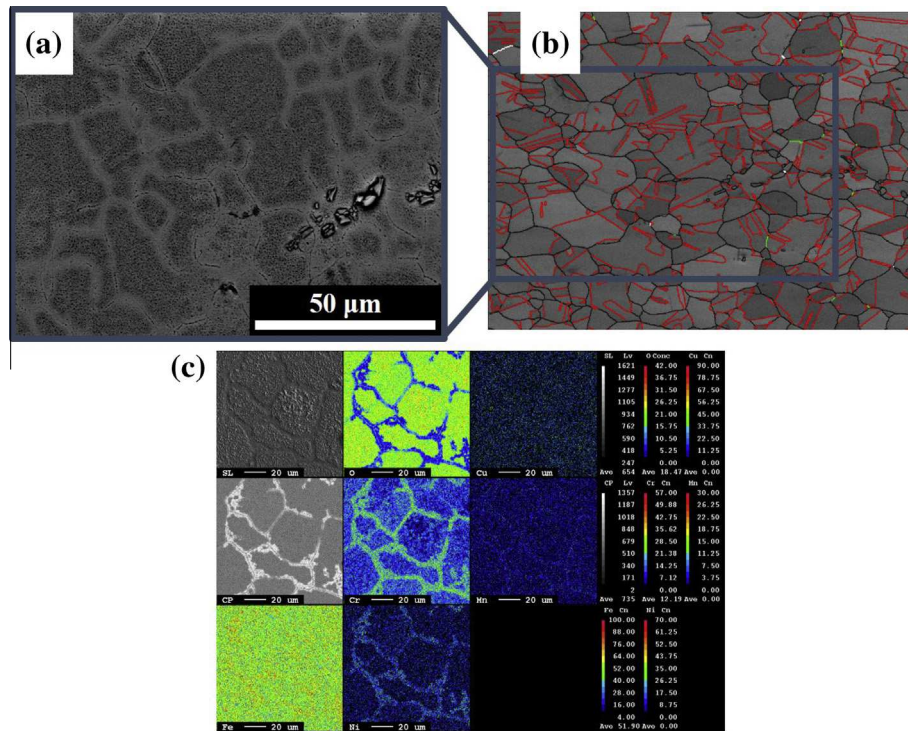


**Fig. 3.** (a) Back scattered electron (BSE) image in the SEM obtained on the surface of the oxide layer formed in the medium grain sample after 30 min of oxidation at 700 °C in air with 20% water vapor. (b) EBSD band contrast map overlaid with grain boundaries, including special boundaries (red:  $\Sigma 3$ , green:  $\Sigma 5$ , white:  $\Sigma 7$ , and black: random boundaries) obtained on the surface before oxidation on the medium grain sample. (c) EPMA mapping obtained on the surface before oxidation obtained on the medium grain sample after 30 min of oxidation at 700 °C in air with 20% water vapor.

(see Fig. 3(b)). The  $\Sigma 3$  CSL grain boundaries that exist inside grains were mostly coherent and did not exhibit selective oxidation. The particles imaged with bright contrast in Fig. 3(a) can be identified as Nb-containing carbide precipitates [7]. Fig. 3(c) shows an EPMA map acquired from the same sample, indicating the presence of O, Fe, Cr, Ni, Mn and Cu. According to the EPMA data, two types of oxides were formed on the outer surface. A Cr-rich oxide was detected at the grain boundaries, where Fe, Mn, and Ni were also found to be enriched. The dark gray regions in Fig. 3(a) were depleted of Cr when compared with the grain boundary region, whereas the intra-grain region contained a higher concentration of O.

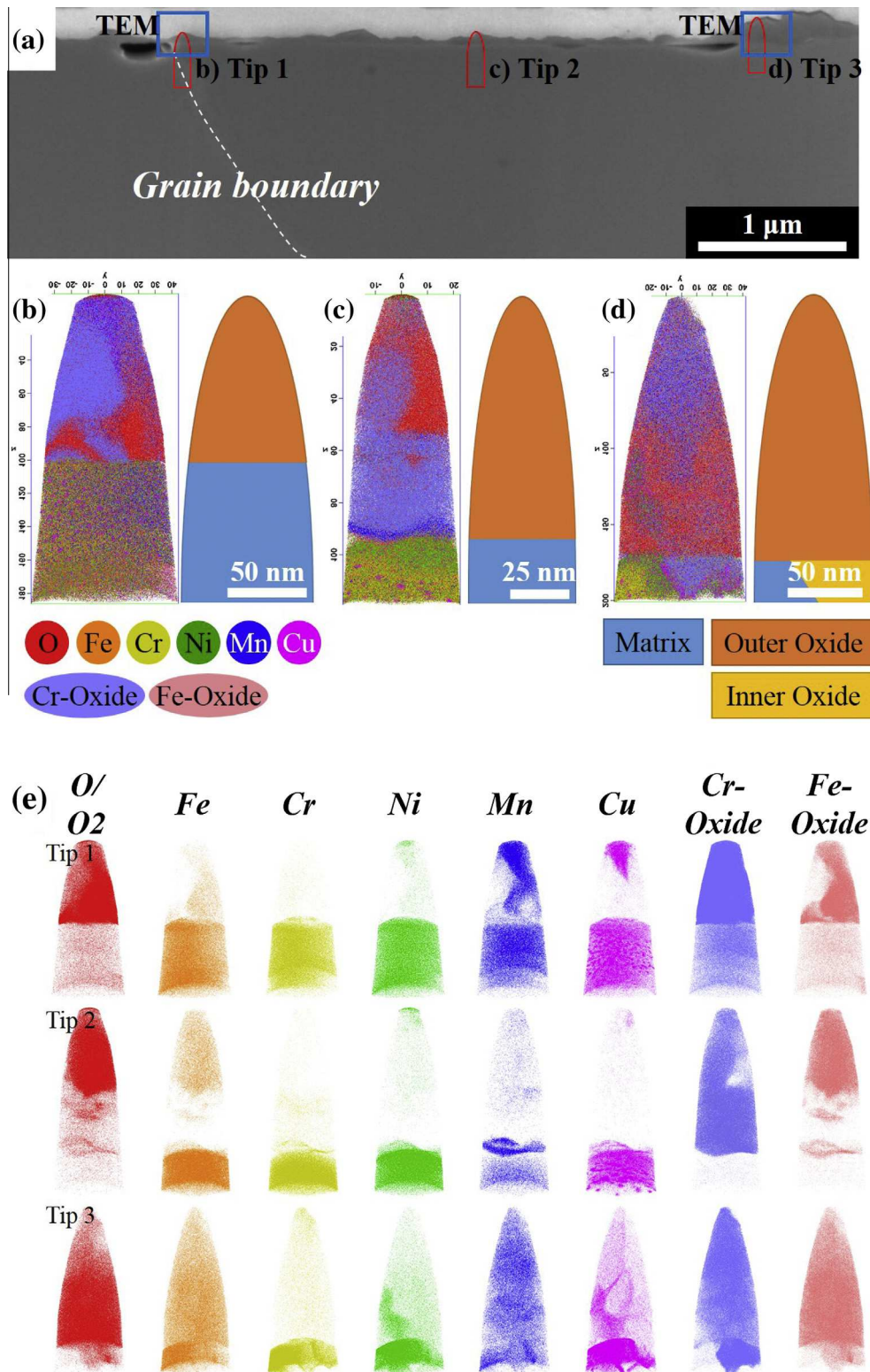
### 3.1.2. Oxide composition analysis using atom probe tomography

Fig. 4(a) shows cross-sectional SEM micrographs of the oxide layer in the medium grain sample after 30 min of oxidation. A thicker oxide formed in the intra-grain regions, whereas a thinner oxide tended to form near the grain boundaries. The oxide thickness was approximately 50–100 nm near the grain boundaries and ~200 nm in the intra-grain region. The outward diffusion of Cr can generate Kirkendall voids at the matrix/oxide interface, which corresponds well with the surface morphologies reported previously [52–55]. Three locations for the APT analysis presented in Fig. 4(a) are schematically marked as (b), (c) and (d). The grain boundary corresponds to the boundary given in Fig. 2(d). The same area was studied using both APT and TEM. 3D atom maps acquired using 3DAPT and schematics drawn to highlight the matrix and oxide regions are presented in Fig. 4(b)–(d). The distribution and enrichment regions of the different elements clearly reveal the outer oxide, inner oxide and matrix regions. Tips 1 and 2 had the outer oxide at the top and the matrix at the bottom. Tip 3 had the outer oxide at the top, whereas the inner oxide and matrix were located at the bottom. A similar dual-layer structure was formed in the intra-grain region of large-grained Fe–Cr–Ni

austenitic stainless steels during long-term oxidation in steam, and the original surface before oxidation was located at the outer/inner oxide interface [56]. Therefore, we suggest that the outer and inner oxide layers grow by the outward diffusion of metal cations and the inward diffusion of oxygen anions, respectively.

APT maps of all three tips are shown in Fig. 4(e). First, the O/O<sub>2</sub> map shows the distribution of oxygen and confirms the presence of outer and inner oxide layers. Moreover, the Cr/Cr oxide and Fe/Fe oxide maps clearly show Cr and Fe enrichments in the outer oxides. Additionally, the Cr oxide map of Tip 3 shows that a Cr-rich oxide layer formed in the inner oxide [30]. Ni was present on the top region in Tips 1 and 2 as part of the protective Ni-coating. Mn was present on the top region, as it diffused through the oxide to the surface to form an external spinel layer [29]. Spherical Cu-rich precipitates of uniform size and homogeneous distribution were detected in the matrix, which agree with previous studies [6,7,57]. Near the surface, the number of Cu-rich precipitates decreased due to the diffusion of Cu to the oxide/gas interface during oxidation. With further oxidation, a Cu-containing spinel structured oxide, Fe<sub>2</sub>CuO<sub>4</sub>, is formed at the top surface of the outer oxide [58].

Regions of interest (ROIs) were clipped from the original APT maps by defining iso-concentration surfaces to perform refined phase analyses. Fig. 5(a)–(c) shows such phase analyses for all three tips. Iso-concentration surfaces of 30 at.% O were chosen to separate the oxide from the matrix region. These oxide and matrix regions were then further divided into parts of different compositions to identify individual phases comprising the oxide and matrix, respectively. The mass spectra of the clipped ROI were analyzed to determine the overall compositions of the phases, where the values are listed in Table 2. Although the analyses were conducted on the same grain boundary, oxides near the grain



**Fig. 4.** (a) Cross-sectional view of the oxide and matrix formed in the medium grain sample after 30 min of oxidation at 700 °C in air with 20% water vapor. (b) 3D atom elemental map displaying the overall distribution and schematic drawing of the regions found in tip 1 (~0.3  $\mu\text{m}$  away from the grain boundary containing over 27 million ions within a volume of  $44 \times 44 \times 186 \text{ nm}^3$ ). (c) Tip 2 (~2  $\mu\text{m}$  away from the grain boundary containing over 14 million ions within a volume of  $22 \times 22 \times 118 \text{ nm}^3$ ). (d) Tip 3 (~4  $\mu\text{m}$  away from the grain boundary containing over 23 million ions within a volume of  $40 \times 40 \times 200 \text{ nm}^3$ ). (e) 3D reconstruction of individual O, Fe, Cr, Ni, Mn, Cu, Cr-oxide (CrO, CrO<sub>2</sub>, CrO<sub>3</sub>) and Fe-oxide (FeO, FeO<sub>2</sub>) ions from all of the tips. (The red (●) dots, orange (●) dots, dark yellow (●) dots, green (●) dots, blue (●) dots, magenta (●) dots, light violet (●) dots and light magenta (●) dots represent oxygen (7.3–100% shown), iron (1.7–10% shown), chromium (30–50% shown), nickel (12–40% shown), manganese (100% shown), copper (52–100% shown), chromium-oxide (10–50% shown), iron-oxide (50–100% shown), respectively.)

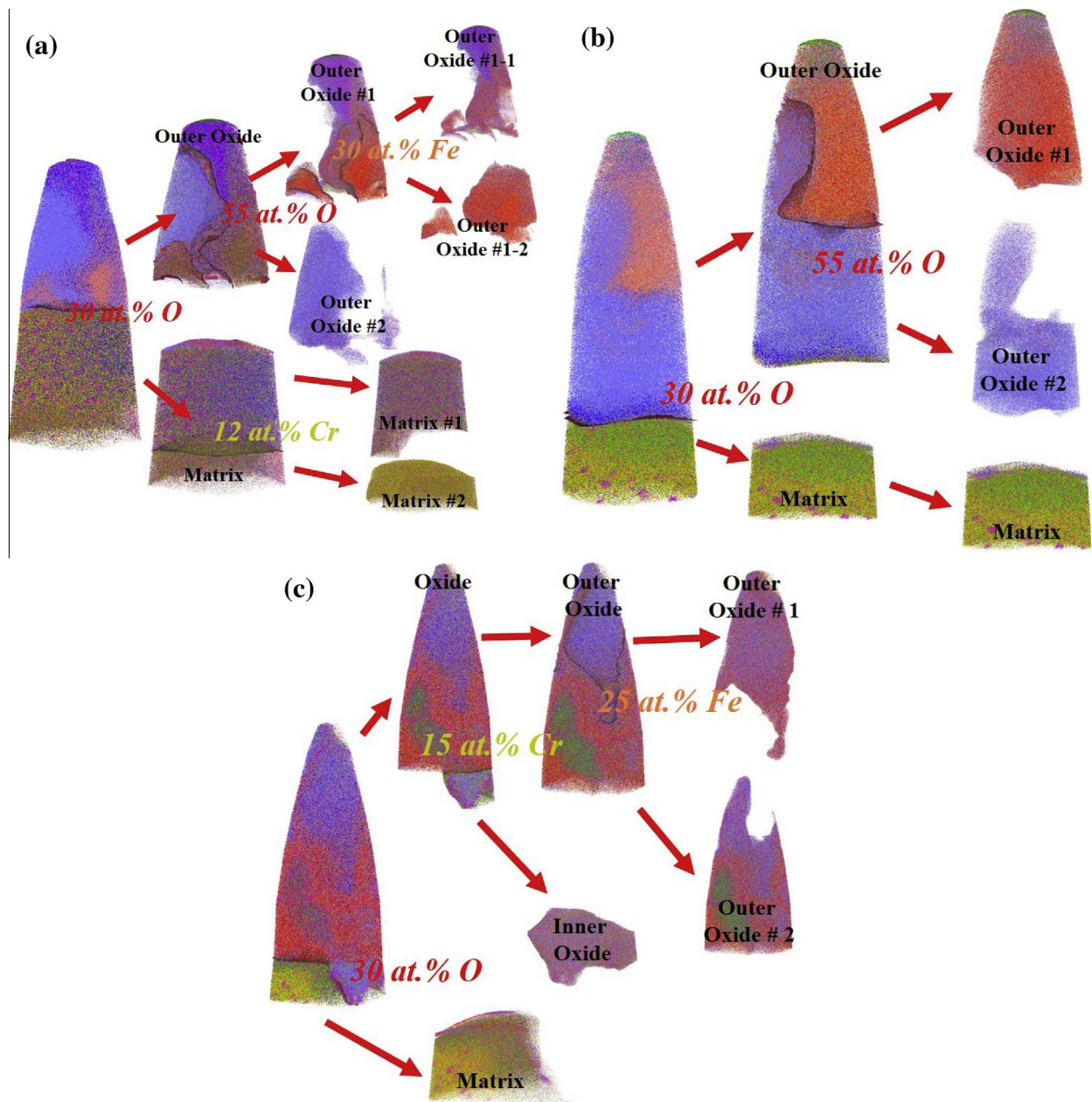


**Fig. 5.** 3D elemental maps of the iso-concentration surface acquired from the original data set (a) Tip 1, (b) Tip 2 and (c) Tip 3. O (red), Fe (orange) and Cr (dark yellow) iso-concentration surfaces are introduced to visualize the positions of the matrix/oxide interface region and the different outer oxide types.

boundary and inter-grain regions exhibited different compositions. Fig. 5(a) shows the outer oxide and matrix region of Tip 1. The outer oxide consisted of three different phases. The outer oxide #1 consisted of Cr-rich (Fe,Mn,Cu) and Fe-rich (Fe,Cr) oxides. The composition of the Cr-rich (Fe,Mn,Cu) oxide in the outer oxide #1-1, which was found near the grain boundary, amounted to 51.5 at.% O, 17.2 at.% Fe, 22.9 at.% Cr, 3.1 at.% Mn and 2.7 at.% Cu. The diffusion of Mn and Cu atoms along the grain boundary is faster than the bulk diffusion in the intra-grain regions. The composition of the Fe-rich (Fe,Cr) oxide in the outer oxide #1-2 was 48.7 at.% O, 38.9 at.% Fe, and 8.23 at.% Cr. The composition of the Cr-rich oxide in the outer oxide #2 was 58.2 at.% O and 38.9 at.% Cr. Whereas the nominal matrix composition of the austenitic stainless steel containing alloyed Cu was 18Cr–9%Ni, the composition of matrix #1 was 64.8 at.% Fe, 16.8 at.% Cr and

12.1 at.% Ni. This slight depletion of Cr and enrichment of Fe and Ni in the matrix #1 region was noticeably enhanced in the matrix #2 region. The Cr depletion and Ni enrichment at the grain boundaries and phase transformation will be discussed elsewhere [59]. Fig. 5(b) shows the outer oxide and matrix region observed in Tip 2. The outer oxide consisted of two different oxide regions. The outer oxide #1 was a Fe-rich (Fe,Cr) oxide of 50.3 at.% O, 39.8 at.% Fe, and 8.05 at.% Cr composition. The outer oxide #2 was Cr-rich oxide with 58.6 at.% O and 39.2 at.% Cr. The matrix composition of Tip 2 was nearly identical to the composition of matrix #1 of Tip 1. Fig. 5(c) shows the outer oxide, inner oxide and matrix region observed in Tip 3. The outer oxide of Tip 3 consisted of two different oxide phases. Both of the phases were (Fe,Cr) oxide, but one was a Cr-rich (Fe,Cr) oxide and the other was a Fe-rich (Fe,Cr) oxide. The composition of these oxides were

**Table 2**Chemical composition (at.%) of the oxides and matrix in each tip shown in Fig. 5 as measured using APT. The error bars represent  $2\sigma$  standard deviation.

		O	Fe	Cr	Ni	Mn	Cu
Tip 1	Outer Oxide #1-1	51.52 ± 0.062	17.25 ± 0.033	22.97 ± 0.045	2.04 ± 0.010	3.10 ± 0.013	2.66 ± 0.012
	Outer Oxide #1-2	48.75 ± 0.083	38.93 ± 0.074	8.23 ± 0.028	1.32 ± 0.011	1.35 ± 0.011	0.27 ± 0.005
	Outer Oxide #2	58.27 ± 0.091	1.79 ± 0.012	38.91 ± 0.071	0.15 ± 0.004	0.23 ± 0.004	0.14 ± 0.003
	Matrix #1	1.81 ± 0.004	64.88 ± 0.032	16.87 ± 0.013	12.17 ± 0.011	0.89 ± 0.002	2.68 ± 0.005
	Matrix #2	0.68 ± 0.005	78.96 ± 0.072	4.53 ± 0.012	13.35 ± 0.024	0.16 ± 0.002	1.71 ± 0.007
Tip 2	Outer Oxide #1	50.31 ± 0.092	39.84 ± 0.087	8.05 ± 0.031	0.99 ± 0.011	0.26 ± 0.005	0.25 ± 0.005
	Outer Oxide #2	58.63 ± 0.095	1.81 ± 0.014	39.21 ± 0.076	0.07 ± 0.002	0.09 ± 0.003	0.03 ± 0.002
	Matrix	0.65 ± 0.005	69.76 ± 0.077	13.25 ± 0.035	11.95 ± 0.036	0.47 ± 0.004	2.58 ± 0.012
Tip 3	Outer Oxide #1	55.96 ± 0.047	19.15 ± 0.021	23.34 ± 0.035	0.46 ± 0.003	0.34 ± 0.003	0.21 ± 0.002
	Outer Oxide #2	52.46 ± 0.025	32.46 ± 0.022	12.03 ± 0.014	1.40 ± 0.003	0.23 ± 0.001	0.50 ± 0.002
	Inner Oxide	51.84 ± 0.051	14.74 ± 0.027	28.45 ± 0.043	2.19 ± 0.009	0.19 ± 0.003	1.01 ± 0.006
	Matrix	2.01 ± 0.009	63.84 ± 0.074	7.27 ± 0.018	22.05 ± 0.033	0.24 ± 0.003	3.55 ± 0.012

55.9 at.% O, 19.1 at.% Fe and 23.3 at.% Cr for outer oxide #1 and 52.4 at.% O, 32.4 at.% Fe and 12.0 at.% Cr for outer oxide #2. The Cr-rich oxide found in Tips 1 and 2 was not found in the outer oxide in Tip 3. The inner oxide beneath the original matrix surface was Cr-rich (Fe,Cr), with 51.8 at.% O, 14.7 at.% Fe, and 28.4 at.% Cr. The matrix composition was 63.8 at.% Fe, 7.27 at.% Cr and 22.0 at.% Ni.

Fig. 6 shows 1D composition profiles across the interfaces between the oxides and matrix in Tips 1–3. The profiles were plotted along cylinders with 15-nm diameters in the directions indicated by the red arrow in Fig. 6. Fig. 6(a) and (c) illustrates that a thin Cr-rich oxide (both outer oxide #2) with a thickness of approximately 40 nm was formed on the matrix. Although the depths of the observed matrix regions were different, the composition profiles were similar. No Ni was detected, indicating that the oxide layer comprises an inner layer of  $\text{Cr}_2\text{O}_3$ . Thinner Fe-rich (Fe,Cr) $_3\text{O}_4$  oxide layers were formed at the top of the outer oxide (see Fig. 6(b) and (c)) and revealed a  $\text{Cr}_2\text{O}_3$  oxide at the bottom of the outer oxide. A strong enrichment of Ni (depletion of Cr) up to 20 nm from the interface was observed in the matrix near the matrix/oxide interface. Ni enrichment at the matrix/oxide interface is correlated with a characteristic Cr-depleted region. This Ni enrichment was previously observed [44] and predicted by quantum chemical molecular dynamics simulation [60]. In Tip 3, the formation of a thicker Fe-rich (Fe,Cr) $_3\text{O}_4$  oxide (outer oxide #1 and #2) was observed (see Fig. 6(d)) because no protective  $\text{Cr}_2\text{O}_3$  oxide was formed on the surface. The composition of the inner oxide layer in Fig. 6(e) corresponds to Cr-rich (Cr,Fe) $_3\text{O}_4$ , where Ni enrichment was also detected at the interface between the matrix and inner oxide layer because of the selective dissolution of Fe and Cr into the oxide; this selective dissolution is due to the lower stability of the Ni-containing oxide compared with that of the Cr- and Fe-containing oxides and the slower diffusion rate of Ni into the oxide [61].

### 3.1.3. Oxide structure analysis using TEM

The local microstructure in the medium grain sample after 30 min of oxidation was studied using TEM bright-field (BF) imaging (see Fig. 7) and the corresponding selected-area diffraction patterns (SADPs). Following the APT analysis presented above, the region analyzed using TEM included both the oxide and original matrix. The region observed using TEM included the same oxide and matrix grains analyzed using APT in the previous section (marked by the blue boxes in Fig. 4(a)). Additionally, both methods probed the same grain boundary; however, the TEM specimen was taken at a slightly different position along the same interface as the APT samples. Fig. 7(a) shows the BF image and SADPs taken near the grain boundary. The BF image contained portions of the grain boundary, matrix and outer oxide. For clarity, the SADPs were

numbered as follows: SADP 1 was taken from the outer oxide just beside grain boundary, and SADP 2 was taken from the next outer oxide. The outer oxides near the grain boundary had inhomogeneous thicknesses between 20 and 50 nm. Both SADPs indicate that the outer oxide layer consisted of rhombohedral crystal structures with zone axis [210], which corresponded to the chemical composition of  $\text{Cr}_2\text{O}_3$  acquired using the APT analysis in the previous section. Fig. 7(b) shows a BF image and SADPs taken from an intra-grain region (4.4  $\mu\text{m}$  away from the grain boundary). The oxide layer formed on this intra-grain region had a double-layer structure, which is consistent with the results reported in a previous study [41]. The interface between the layers is clearly identified as a nearly straight line between the two regions with different contrasts. SADP 3 was taken from the outer oxide 4.4  $\mu\text{m}$  away from the grain boundary, and SADP 4 was taken from the inner oxide beneath the oxide of SADP 3. The intra-grain outer oxide had a thickness of 100 nm and exhibited a spinel crystal structure with zone axis [111]. The chemical composition acquired using APT analysis corresponded to  $\text{Fe}_2\text{CrO}_4$ . The inner oxide formed beneath the outer oxide was thinner (~50 nm) than the outer oxide and exhibited the same spinel crystal structure with zone axis [100]. The chemical composition acquired using APT analysis corresponded to  $\text{FeCr}_2\text{O}_4$ . The TEM results revealed that the outer and inner oxides of the intra-grain area had a similar spinel crystal structure even though both oxides had different chemical compositions.

## 3.2. Oxidation behavior up to 28 h

### 3.2.1. Grain size and CSLB analysis using EBSD

In Fig. 8, the average grain sizes of all samples before oxidation were determined using EBSD maps. The average grain size and number fraction of CSL grain boundaries were obtained from the average of three different areas in each specimen [41]. As shown in Fig. 3, the  $\Sigma 3$  CSL grain boundaries exhibited the same oxidation behavior as the intra-grain region. Furthermore, only high-angle grain boundaries will be considered in the following discussion of the role of grain boundaries in the oxidation kinetics. Therefore, between the average grain sizes presented in Fig. 8, neglecting the  $\Sigma 3$  CSL grain boundaries, the values were determined to be 27, 17 and 8  $\mu\text{m}$  for the large grain, medium grain and small grain samples, respectively. The  $\Sigma 3$  CSL grain boundary fractions observed for all samples remained similar and more than 50% of the total grain boundary line fraction.

### 3.2.2. Mass gain analysis for the study of oxidation kinetics

The growth kinetics of the oxide layers formed on the steels was investigated by measuring the mass gain per unit area versus oxidation time. Fig. 9 illustrates that there was a clear difference in the

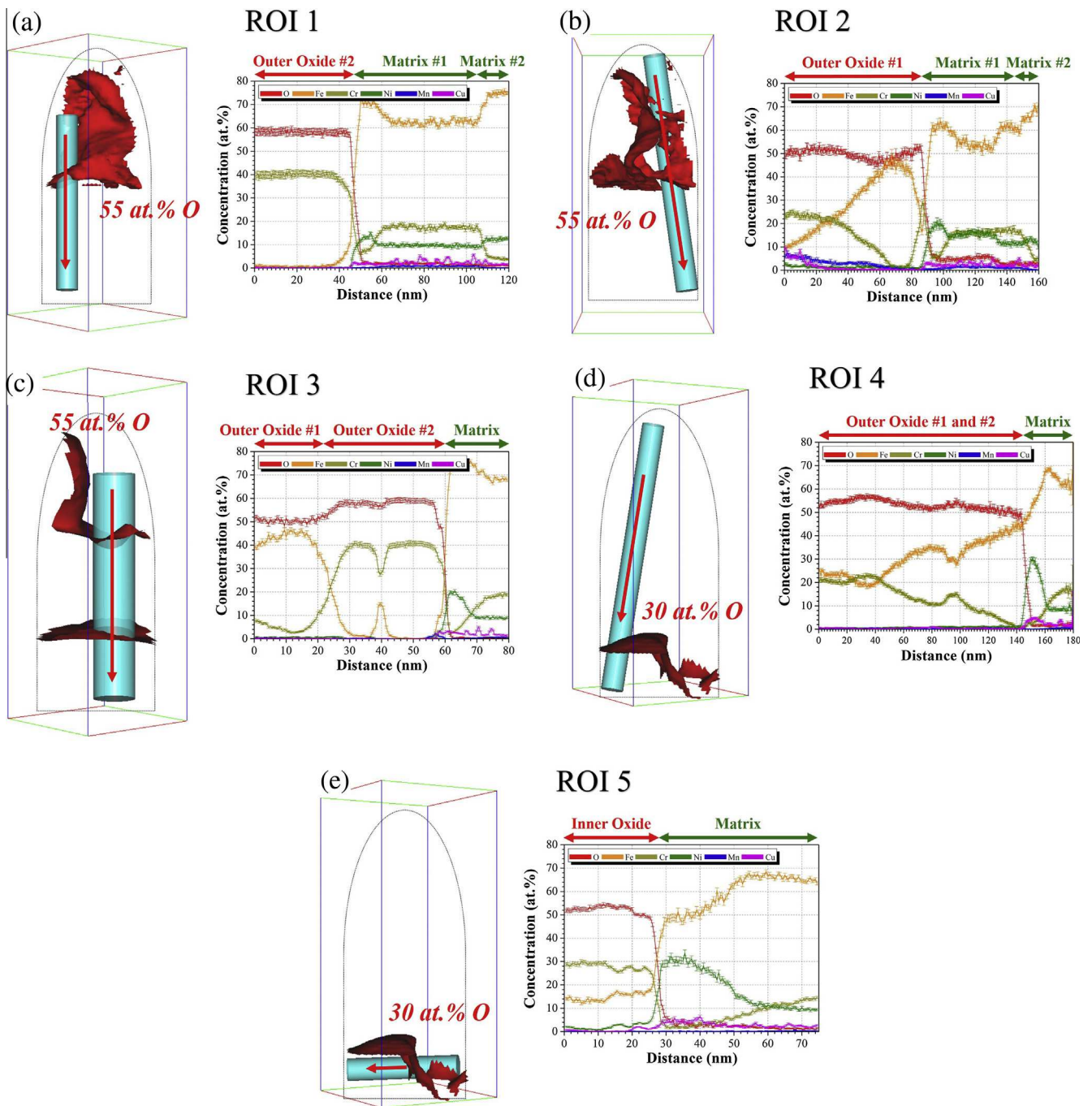


**Fig. 6.** Elemental concentration 1D profiles (fixed bin width of 0.5 nm) along the region of interest (ROI) taken across the oxide and matrix from Tip 1 (a) and (b), Tip 2 (c) and Tip 3 (d) and (e). O (red) iso-concentration surfaces are introduced to visualize the positions of the matrix/oxide interface region and the different outer oxide types. 1D profiles of all tips determined within a cylinder with a diameter of 15 nm. The red arrows mark the directions in which the concentration profiles are drawn. The error bars represent  $\sigma$  statistical error due to the limited number of atoms in the sample volume.

oxidation rates depending on the grain size of the samples. Fig. 9(a) presents the mass gain curves of the austenitic stainless steels containing alloyed Cu with different grain sizes oxidized at 700 °C in air with 20% water vapor for 28 h. Slight oxide spallation during cooling to room temperature occurred for the large grain sample. The curves illustrate that the small grain sample, which has the smallest average grain size (8  $\mu\text{m}$ ), has the largest mass gain among all samples after 2 h of oxidation. However, for times beyond 2 h, the mass gain decreased drastically and approached a saturation level, indicating stable oxidation in the oxidation

resistance. In contrast, the large grain and medium grain samples exhibited a lower mass gain compared with the small grain sample for oxidation times  $\leq 2$  h, whereas the mass gain of both samples was larger than in the small grain sample for more than 2 h of oxidation. This large value likely results from the formation of non-protective Fe-rich oxides in the intra-grain region. Therefore, a critical grain size appears necessary to cover the surface with a protective  $\text{Cr}_2\text{O}_3$  oxide, which will be discussed later in more detail. All mass gain curves exhibited a strong increase during the initial stage of oxidation ( $\leq 1$  h), followed by a decrease in

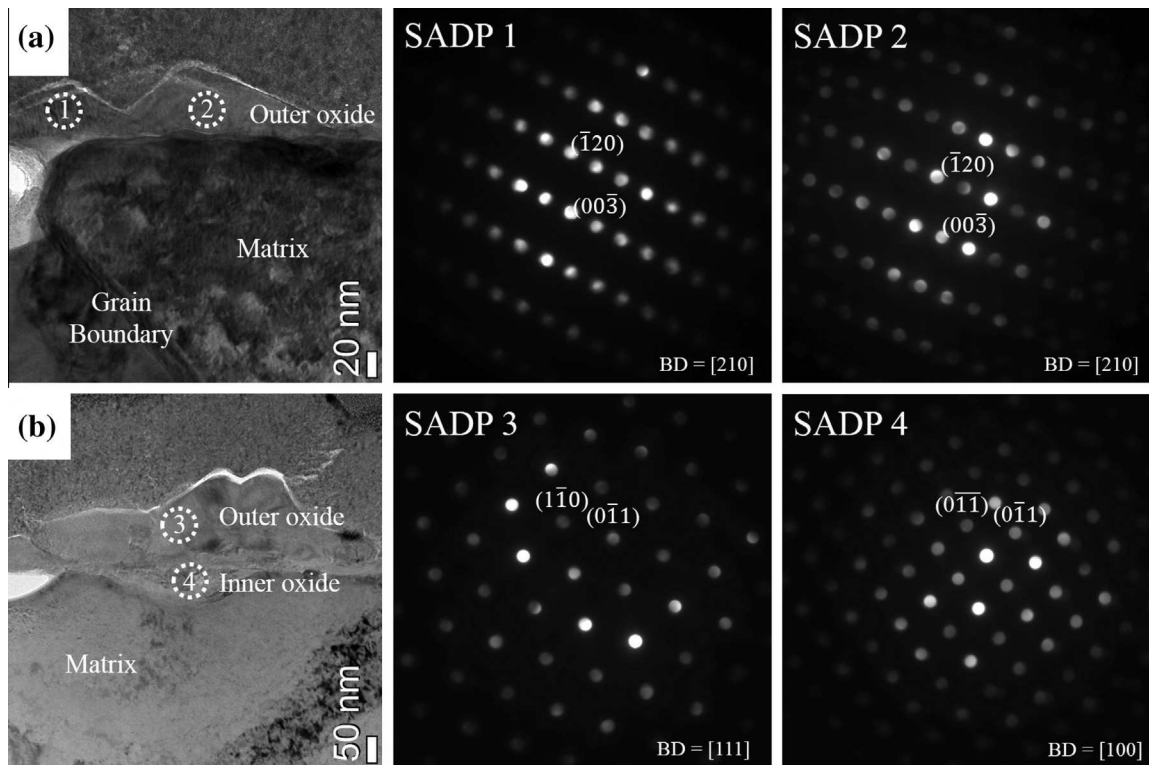


**Fig. 7.** TEM micrographs and the corresponding SADP taken obtained in the medium grain sample after 30 min of oxidation at 700 °C in air with 20% water vapor. (a) Cross sectional TEM image of the oxide layer composed on the near grain boundary region (SADP 1 and 2:  $\text{Cr}_2\text{O}_3$  with zone axis of  $[210]$ ). (b) Cross-sectional TEM image of the oxide layer on the intra-grain region (SADP 3:  $\text{Fe}_2\text{CrO}_4$  with zone axis of  $[111]$ , SADP 4:  $\text{FeCr}_2\text{O}_4$  with zone axis of  $[100]$ ).

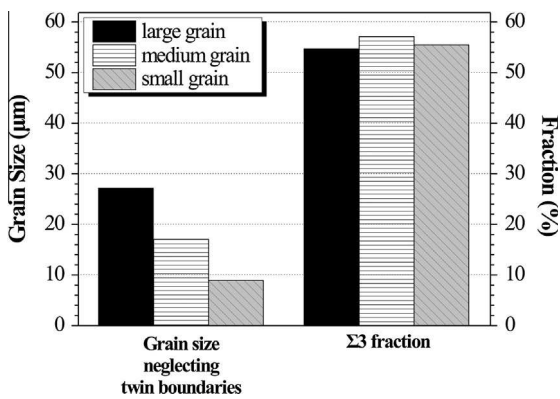


**Fig. 8.** Comparison of the large grain, medium grain and small grain samples in terms of grain size and  $\Sigma 3$  boundary number fraction.

the mass gain in the later stages of oxidation. In the previous study [41], we reported that the mass gain after 500 h of oxidation that was observed for the small grain sample was three times smaller than that of the medium grain sample and more than seven times smaller than that of the large grain sample. The mass gain curves follow a parabolic rate law given by  $(\Delta M/S)^2 = A + K_p t$  [62–64], where  $\Delta M$  is the mass gain,  $S$  is the unit area,  $A$  is a constant,  $K_p$  is the parabolic rate constant and  $t$  is time. We plotted the square of mass gain versus time to determine the parabolic rate constant, which indicates the changes in the oxidation mechanism. Fig. 9(b) illustrates that during the first regime (0–2 h), the parabolic rate constants  $K_p$  of the small grain sample are similar to the values found for the growth of the  $\text{Cr}_2\text{O}_3$  oxide in 18/8 type stainless steels [65]. In the small grain sample, a straight line was observed after

the first regime ( $\sim 2$  h), and no evidence of a transition in the oxidation kinetics was observed. In contrast, for the large grain and medium grain samples, the parabolic rate constants  $K_p$  exhibited continuously increasing slopes after the first stage. The early stage oxidation kinetics was highly similar for both samples. The parabolic constants determined for the second regime (2–12 h) correspond well with the value of Fe-rich oxides reported in a previous study [33]. The rate constants  $K_p$  determined from the slope of the linear plots in the first and second stages are presented in Table 3. Between 2 h and 12 h of oxidation, the plots in Fig. 9(b) can be fitted with straight lines, where rate constant values of  $0.05018 \text{ g}^2 \text{ cm}^{-4} \text{ h}^{-1}$ ,  $0.04868 \text{ mg}^2 \text{ cm}^{-4} \text{ h}^{-1}$  and  $0.00574 \text{ mg}^2 \text{ cm}^{-4} \text{ h}^{-1}$  are calculated for the large grain, medium grain and small grain samples, respectively. Thus, the oxidation rates after 2 h of oxidation at 700 °C in air with 20% water vapor decrease in the following order: large grain > medium grain > small grain.

### 3.2.3. Oxide surface morphology analysis using SEM

The SEM images in Fig. 10 show the surfaces of the medium grain and small grain samples prior to oxidation and also after oxidation for 6 and 12 h, respectively. For the medium grain sample, our previous investigation with EDS [41] illustrated that the oxide layer consisted of two different oxide complexes after 500 h of oxidation. The overall oxide surface morphology of the medium grain sample was highly similar to that of the large grain sample. The thicker nodule-like features on the surface of intra-grain regions were Fe-rich oxides, and the bottom regions near the grain boundaries were thin Cr-rich oxides. Such selective oxidation behavior was also reported by other authors [18,19,25,27] in austenitic stainless steels using EDS analysis. The nodules also became progressively enriched in Fe, and the number density of nodules that formed increased upon further oxidation. Fig. 10(a) shows that Fe-rich nodules only form on the intra-grain regions. However,

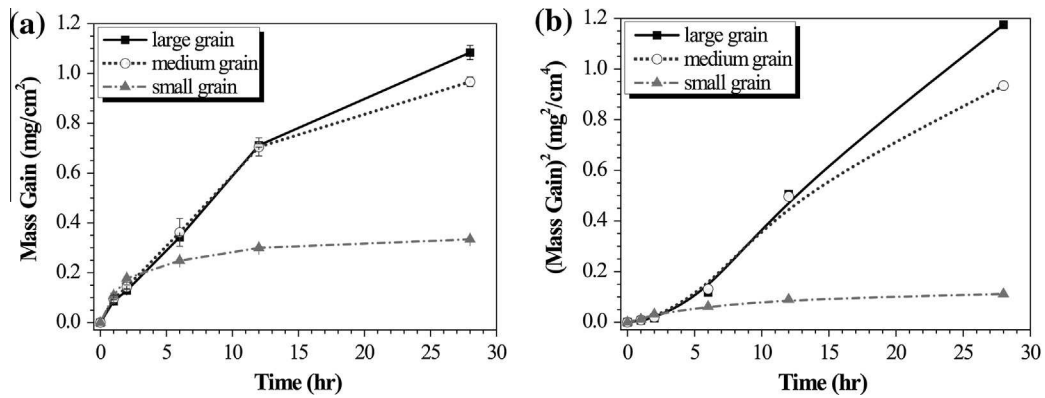


**Fig. 9.** (a) Mass gain vs. time curve. (b) Quadratic function of the mass gain vs. time curve obtained for the large grain, medium grain and small grain samples over 28 h of oxidation at 700 °C in air with 20% water vapor [41]. The average grain sizes of the samples (not including the  $\Sigma 3$  boundaries) were 27, 17 and 8  $\mu\text{m}$  for the large grain, medium grain and small grain samples, respectively.

**Table 3**  
Calculated parabolic rate constants.

Samples	Parabolic rate constant ( $\text{mg}^2 \text{cm}^{-4} \text{h}^{-1}$ )
Large grain (27 $\mu\text{m}$ )	0.00826 (0–2 h), 0.05018 (2–12 h)
Medium grain (17 $\mu\text{m}$ )	0.01022 (0–2 h), 0.04868 (2–12 h)
Small grain (8 $\mu\text{m}$ )	0.01581 (0–2 h), 0.00574 (2–12 h)

they did not form on every grain, and they never formed on grain boundaries, indicating the size and distribution of these nodules depend on the matrix grain structure. Single nodules within the same intra-grain region tended to agglomerate and merged as the oxidation time was increased. As noted previously, the surface was not covered entirely by Fe-rich outer oxide nodules, but spallation occurred in some places. In contrast, the entire surface of the small grain sample was covered with only Cr-rich oxides (see Fig. 10(b)). The oxide formed over the entire surface was a thin, adherent oxide layer similar to that formed over grain boundaries of the medium grain sample. No Fe-rich nodules formed on the surface of the small grain sample.

### 3.2.4. Phase analysis using X-ray diffraction

The XRD patterns of samples oxidized for 12 h are shown in Fig. 11. Based on several previous studies, the presence of the  $\gamma$ -Fe (Joint Committee Powder Diffraction Standard file: JCPDS 33-0397),  $\alpha$ -Fe (JCPDS 85-1410),  $\text{Cr}_2\text{O}_3$  (JCPDS 38-1479),  $\text{Fe}_2\text{O}_3$  (JCPDS 33-0664),  $\text{Mn}_{1.5}\text{Cr}_{1.5}\text{O}_4$  (JCPDS 33-0892),  $\text{FeCr}_2\text{O}_4$  (JCPDS 34-0140) and  $\text{CuFe}_2\text{O}_4$  (JCPDS 25-0283) spinel phases during high-temperature oxidation were confirmed [11,17,58]. Fig. 11(a) shows  $\text{Cr}_2\text{O}_3$  peaks, which appear with the  $\text{Mn}_{1.5}\text{Cr}_{1.5}\text{O}_4$  peaks from the beginning of the oxidation in the large grain sample. Peaks belonging to the austenite matrix were still observed because of the low thickness of the oxide layers. Phase transitions at the sample surface were observed after 6 h of oxidation. The initially formed oxides ( $\text{Cr}_2\text{O}_3$  and  $\text{Mn}_{1.5}\text{Cr}_{1.5}\text{O}_4$ ) disappeared completely, and only peaks belonging to Fe-containing oxides, such as  $\text{Fe}_2\text{O}_3$  and  $\text{FeCr}_2\text{O}_4$ , were observed. Fig. 11(b) shows that in the medium grain and large grain samples,  $\text{Cr}_2\text{O}_3$  was initially formed followed by  $\text{Fe}_2\text{O}_3$  during the later stages. Additionally, a peak pertaining to austenite was observed because the Fe-rich oxide did not cover the entire surface after oxidation for 12 h, as shown in the SE image in Fig. 10(a). Fig. 11(c) shows the XRD patterns of the small grain sample, which revealed that a  $\text{Cr}_2\text{O}_3$  layer was immediately formed

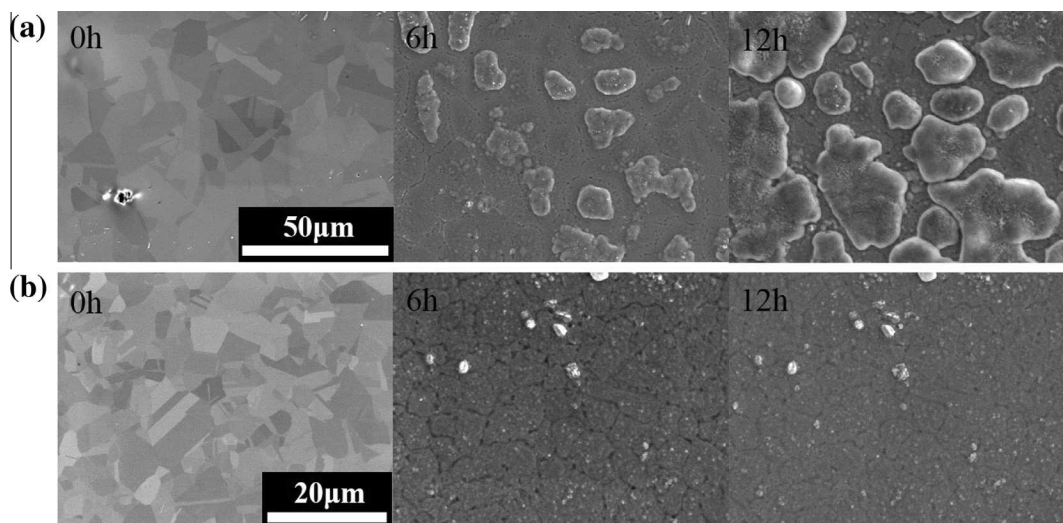


**Fig. 10.** Secondary electron (SE) images obtained on the surface of the oxide layer formed after oxidation at 700 °C in air with 20% water vapor. (a) Medium grain and (b) small grain samples. The average grain sizes (not including the  $\Sigma 3$  boundaries) were 17 and 8  $\mu\text{m}$  for the medium grain and small grain samples, respectively.

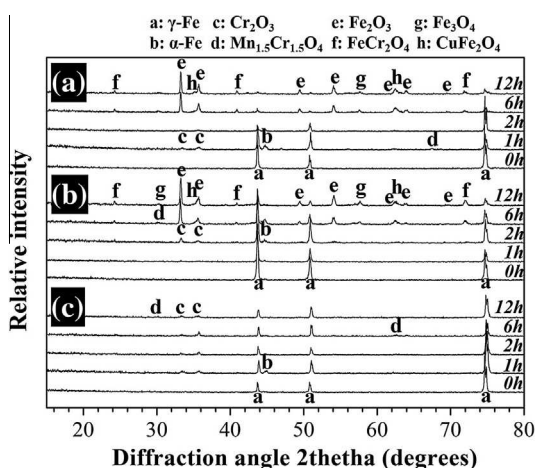


**Fig. 11.** XRD analysis of the oxides performed on (a) large grain, (b) medium grain and (c) small grain samples over 12 h of oxidation at 700 °C in air with 20% water vapor. The average grain sizes of the samples (not considering the  $\Sigma 3$  boundaries) were 27, 17 and 8  $\mu\text{m}$  for the large grain, medium grain and small grain samples, respectively.

with  $\text{Mn}_{1.5}\text{Cr}_{1.5}\text{O}_4$  at the beginning of the oxidation. No Fe-containing oxides were formed until the end of the oxidation test.

## 4. Discussion

### 4.1. Initial stage oxidation (~30 min)

#### 4.1.1. Oxidation of the surface and grain boundary regions

The cross-sectional oxide layer distribution in the medium grain sample after 30 min of oxidation is shown in Fig. 12. APT (as shown in Figs. 5 and 6) and TEM (as shown in Fig. 7) analyses indicate that the outer oxide layer consists of a Fe-rich oxide and Cr-rich oxide with a rhombohedral crystal structure. The outer oxide layer probed near random high angle grain boundaries is thin (90–100 nm thick, as shown in Fig. 4), but it still has a duplex-layer structure. The layers are mainly composed of protective  $\text{Cr}_2\text{O}_3$  with a Fe-rich  $(\text{Fe,Cr})_3\text{O}_4$  oxide on top, which contains small amounts of Ni, Mn and Cu. The formation of a uniform protective oxide can be clearly observed in Fig. 3. This protective oxide layer begins to form along the grain boundaries but not in the intra-grain region. Furthermore, this layer prevents inner oxidation in the matrix and acts as a diffusion barrier against oxygen. In contrast, the outer oxide layer that formed  $\sim 4 \mu\text{m}$  away from the random grain boundaries consists of a thick Fe-rich  $(\text{Fe,Cr})_3\text{O}_4$  oxide with a spinel crystal structure containing small amounts of Ni, Mn and Cu. Furthermore, an inner oxide layer with a stoichiometry of  $\text{FeCr}_2\text{O}_4$  is formed beneath original surface, which has the same spinel crystal structure. Because there is no protective  $\text{Cr}_2\text{O}_3$ , these oxide layers grow continuously and form a thicker outer oxide and inner oxide layer in the later stage of oxidation [41].

Ni is present throughout the oxide layer (as shown in Fig. 4(e)) and is also enriched at the matrix/oxide interface (as shown in Fig. 6). Wood [66] observed that small amounts of Ni enter the

oxide layer in Ni–Cr alloys, although it exhibits relatively weak chemical attraction to oxygen compared with Cr. Ni enrichment at the matrix/oxide interface could be related to the different diffusion rates because the lattice diffusion rate of Ni is reported to be slower than that of Cr and Fe in Fe–Cr–Ni alloys ( $D_{\text{Cr}} > D_{\text{Fe}} > D_{\text{Ni}}$ ) [67]. Although the origin of the Ni enrichment is not clear, this result reveals that selective diffusion of Fe and Cr occurs at the matrix/oxide interface.

Minor amounts of Mn and Cu are also detected in the outer oxide layer. Mn is locally enriched in the outer oxide, as detected using APT. Caplan et al. [68] showed that Mn has a detrimental effect on the oxidation resistance of ferritic stainless steels because of the formation of a  $(\text{MnCr})_3\text{O}_4$  spinel phase. Although the Mn content in the austenitic stainless steel containing alloyed Cu as studied here is relatively low, the presence of Mn in the outer oxide can be explained by the relatively fast diffusion of Mn through the  $\text{Cr}_2\text{O}_3$  oxide [69]. The formation of the  $(\text{MnCr})_3\text{O}_4$  spinel oxide on top of a  $\text{Cr}_2\text{O}_3$  oxide layer is generally observed due to the outward diffusion of Mn from the bulk through the  $\text{Cr}_2\text{O}_3$  oxide [70]. According to the APT analysis results from the outer oxide #1 of Tip 1 in Figs. 4 (e) and 6 (b), Mn is enriched in the outer oxide, especially along the grain boundary of the oxide. This rapid Mn diffusion along the grain boundary of the  $\text{Cr}_2\text{O}_3$  layer indicates the formation of a Mn-rich oxide on the outer surface of the  $\text{Cr}_2\text{O}_3$  layer.

The APT analysis result also indicates the enrichment of Cu at the top surface of the outer oxide. This observation coincides with author's previous observation that the Cu addition in austenite stainless steel induces Cu-containing spinel oxides on the top surface after long-term oxidation [58].

#### 4.1.2. Initial oxidation mechanism

In the initial stage of oxidation, metal cations in the alloy and oxygen in the ambient gas react to form an oxide layer, where the oxidation mechanism is strongly dependent on the thermodynamic and kinetic boundary conditions. The relative thermodynamic stability of the oxides should be considered in the thermodynamic predictions. Regarding the  $\Delta G^0$ – $T$  curves obtained by Ellingham–Richardson (Fig. 13(a)), the free enthalpy  $\Delta G^0$  of  $\text{Cr}_2\text{O}_3$  is far more negative than  $\Delta G^0$  for  $\text{FeO}$ ,  $\text{Fe}_2\text{O}_3$  or  $\text{Fe}_3\text{O}_4$  at temperatures below 1300 K. The Gibbs free energies of the  $\text{Fe}_2\text{O}_3$  and  $\text{Cr}_2\text{O}_3$  oxides are approximately  $-310$  and  $-580$  kJ/mol, respectively, at 973 K. Thus, the formation of  $\text{Cr}_2\text{O}_3$  is thermodynamically favored. The oxide layer formed on austenitic stainless steels is also predicted using thermodynamic calculations using the FactSage software and the FactPS, FToxide and FTLite databases. Fig. 13(b) shows the calculation results of the phase stabilities for Fe–Cr–Ni steels at 700 °C according to the oxygen partial pressure and Cr concentration. In this condition,  $\text{Cr}_2\text{O}_3$  is present at the lowest oxygen potential, whereas  $\text{Fe}_3\text{O}_4$  and  $\text{FeCr}_2\text{O}_4$  become stable with increasing oxygen partial pressure and  $\text{Fe}_2\text{O}_3$  and  $\text{FeCr}_2\text{O}_4$  mainly exist at high oxygen partial pressures. From this calculation, a layered structure of mixed oxides was expected in the Fe–Cr–Ni steels. In terms of oxidation kinetics for such Cr-containing alloy, the outward diffusion of cations from the alloy and the inward diffusion of oxygen from the ambient gas compete against each other.

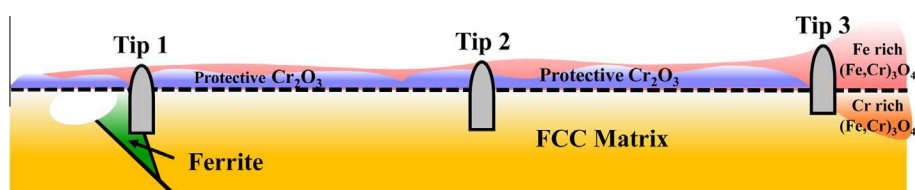


**Fig. 12.** Schematic representation of the oxide layer formed on the surface of the medium grain sample after 30 min of oxidation at 700 °C in air with 20% water vapor.

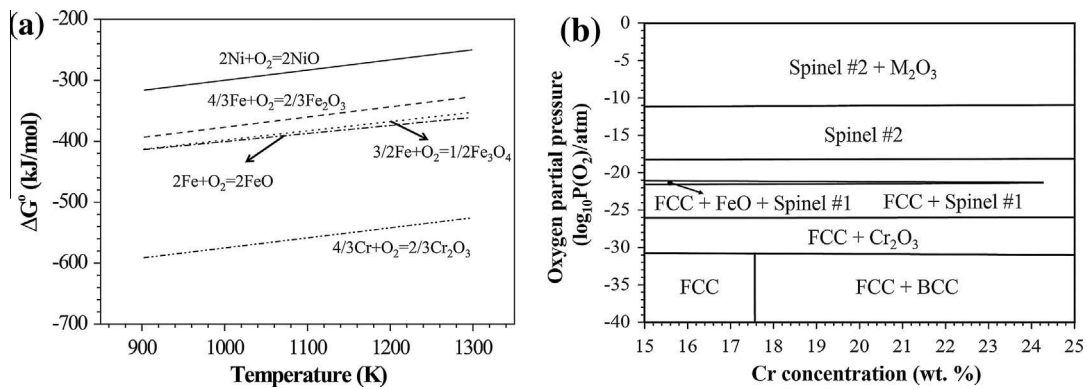


**Fig. 13.** (a) Ellingham diagram showing the standard free energy ( $\Delta G^0$ ) with temperature for the oxidation of Fe, Cr and Ni. (b) The phase stabilities for Fe–Cr–Ni steels at 700 °C as a function of the oxygen partial pressure and corresponding Cr concentration (thermodynamic calculation using FactSage). Spinel #1:  $\text{Fe}_3\text{O}_4$  and  $\text{FeCr}_2\text{O}_4$ , Spinel #2:  $\text{Fe}_3\text{O}_4$ ,  $\text{FeCr}_2\text{O}_4$  and  $\text{FeNi}_2\text{O}_4$ ,  $\text{M}_2\text{O}_3$ :  $\text{Cr}_2\text{O}_3$  and  $\text{Fe}_2\text{O}_3$ .

The bulk diffusion coefficient of O is close to that of Cr, but the grain boundary diffusion coefficient of Cr is several orders of magnitude higher than that of O in  $\text{Cr}_2\text{O}_3$  [71]. These results are in good agreement with the observation that  $\text{Cr}_2\text{O}_3$  was presented as an outer oxide after high-temperature oxidation at the near grain boundary regions. Because  $\text{Cr}_2\text{O}_3$  formation is favored at all temperatures, the presence of an Fe oxide on top of the outer oxide layer in the initial oxidation stage at 700 °C requires an explanation. The duplex-layer oxide is formed because the oxidation procedure is kinetically controlled rather than thermodynamically preferred due to rapid metal cation diffusion through the oxide. Once the formation of the protective  $\text{Cr}_2\text{O}_3$  layer is complete, the oxidation kinetics are controlled by diffusion through the oxide layer. The diffusion coefficients ( $D$ ) decrease in the order  $D_{\text{Mn}} > D_{\text{Fe}} > D_{\text{Ni}} > D_{\text{Cr}}$  in the  $\text{Cr}_2\text{O}_3$  layer [72]. The outer spinel layer formed at high temperatures is due to the outward diffusion of cations, such as Fe, Ni, Mn and Cu, from the alloy through the  $\text{Cr}_2\text{O}_3$  layer. Additionally, an Fe-rich oxide can be formed, which grows at a significantly faster rate than the Cr-rich oxide ( $\text{FeO}:\text{Cr}_2\text{O}_3 = 1:10^{-5}$ ) [73,74]. During the oxidation process,  $\text{Cr}_2\text{O}_3$  was first formed on the surface. At the same time, Fe also reacted with O to form FeO. FeO is thermodynamically more stable than  $\text{Fe}_2\text{O}_3$  and  $\text{Fe}_3\text{O}_4$ . Thus, the Fe-rich oxide observed in Fig. 6(b) and (c) represents the outer oxide with  $\text{Cr}_2\text{O}_3$  after initial oxidation. The outward diffusion of Fe, which is blocked by the protective  $\text{Cr}_2\text{O}_3$  layer, prevents further formation of an Fe-containing oxide near the grain boundaries. The protective  $\text{Cr}_2\text{O}_3$  layer cannot be easily detected in Tip 3, as observed in Fig. 6(d). Instead, the formation of a non-protective Fe oxide is observed because of the favorable reaction of  $\text{FeO}(\text{s}) + \text{Cr}_2\text{O}_3(\text{s}) = \text{FeCr}_2\text{O}_4(\text{s})$  [75]. The transition from a protective  $\text{Cr}_2\text{O}_3$  oxide to a non-protective Fe-rich oxide is governed by the outward diffusion of Fe through the loose  $\text{Cr}_2\text{O}_3$ . Additionally, it should be also considered that the initially formed  $\text{Cr}_2\text{O}_3$  can be evaporated as  $\text{Cr}_2\text{O}_3$  gas molecules when it reacts with oxygen gas. Because the oxidation test was carried out in air with 20% water vapor, the evaporation of  $\text{Cr}_2\text{O}_3$  can be more serious. Water vapor together with oxygen gas reacts with  $\text{Cr}_2\text{O}_3$  and forms gaseous chromium hydroxide species such as  $\text{Cr}_2\text{O}_3(\text{OH})_2$  and  $\text{Cr}_2\text{O}_3(\text{OH})$ , which enhances the instability of  $\text{Cr}_2\text{O}_3$  layer [82]. For the inner oxide, oxide layer with a spinel crystal structure gradually developed because the inward diffusion of O is also favorable in Fe-rich oxides.

## 4.2. Oxidation up to 28 h

### 4.2.1. Grain refinement effect

The compositions and morphologies of the oxide layers observed on the austenitic stainless steel containing alloyed Cu

are similar to observations by other researchers for steels with similar compositions [22]. In the first regime of the early stage oxidation process ( $\sim 2$  h), the oxidation behavior of all samples can be described by the formation of  $\text{Cr}_2\text{O}_3$  followed by the surface diffusion of Cr and the associated spreading of  $\text{Cr}_2\text{O}_3$  from the grain boundaries toward the intra-grain regions. According to Fig. 9, the oxidation kinetics of the samples did not follow a perfect parabolic law, i.e.,  $(\Delta M/S)^2 = A + K_p t$  [62–64]. Only the small grain sample appeared to enter the parabolic regime after 6 h of oxidation. Nevertheless, we can deduce the oxidation kinetics of each sample and a relevant diffusion rate of ions through the oxide from the slope in Fig. 9(b). Because the grain size of the small grain sample is smaller than that of the large grain and medium grain samples, the volume fraction of the grain boundary area of the small grain sample is larger than that of the other samples. Thus, the oxidation rate of the small grain sample is faster than that of other samples during the first regime (0–2 h) of early stage oxidation. For the large grain and medium grain samples, two different stages of oxidation behavior can be identified from the slope change in Fig. 9(b), which indicates a change in the parabolic constant. The oxidation rate during the first regime is slower than during the second regime (2–12 h) of early stage oxidation. The different parabolic rate constants in the same sample are related to the different types of oxide formation. This observation is in agreement with the kinetics, surface morphology and XRD data shown in Figs. 9–11 after 2 h of oxidation.

The oxidation behavior of the large-grained sample is determined by both outward diffusion of metal cations (mainly as  $\text{Fe}^{2+}$  and/or  $\text{Fe}^{3+}$ ), resulting in outer oxide growth, and inward oxygen anion diffusion ( $\text{O}^{2-}$ ), which results in inner oxide growth. The outward diffusion of Fe is closely related to the amount of Cr supplied to the oxide. In the case of an insufficient Cr supply to the intra-grain region, a fully dense protective  $\text{Cr}_2\text{O}_3$  oxide cannot be formed, which results in the continuous diffusion of Fe ion to the surface and allows for the formation of a thick Fe-rich oxide layer. Due to the relatively high growth rate of the Fe-rich oxide layer [74], the entire surface of the material is readily covered by an Fe-rich oxide. Whereas the Fe-rich oxide contains  $\text{Fe}_3\text{O}_4$  and  $\text{Fe}_2\text{O}_3$  in the outer oxide, Cr-rich  $\text{FeCr}_2\text{O}_4$  spinel oxides form in the inner oxide layer. An effective diffusion coefficient ( $D_{\text{eff}}$ ) of Cr is obtained from the weighted average of the bulk ( $D_L$ ) and the grain boundary ( $D_{\text{GB}}$ ) diffusion coefficients as follows [76]:

$$D_{\text{eff}} = (1 - f)D_L + fD_{\text{GB}} \quad (1)$$

where  $f$  is the volume fraction of the grain boundaries. When assuming that the grains are cubic, i.e.,  $f = \frac{2\delta}{d}$  and  $D_{\text{GB}} \gg D_L$ , and  $d$

and  $\delta$  are the grain size and width of the grain boundary region, respectively, Eq. (1) can be simplified as follows [12]:

$$D_{eff} = D_L + \frac{2\delta}{d}(D_{GB} + D_L) \approx D_L + \frac{2\delta}{d}D_{GB} \quad (2)$$

Therefore,  $D_{eff}$  increases with decreasing grain size  $d$ .

These equations were used to interpret the present data. In this study, the grain sizes of the samples, when neglecting the  $\Sigma 3$  CSL grain boundaries, were 27, 17 and 8  $\mu\text{m}$  for the large grain, medium grain and small grain samples, respectively.  $D_{GB}/D_L$  is assumed to be  $10^5$  according to Atkinson [77], who showed that the ratio of the bulk to the grain boundary diffusion coefficients is in the range of  $10^4$ – $10^6$ , and  $\delta$  is assumed to be 0.5 nm [78]. The ratios of  $D_{eff}^{MC}/D_{eff}^{LC}$  and  $D_{eff}^{SG}/D_{eff}^{LG}$  are calculated to be 1.44 and 2.87, respectively. This estimate shows that  $D_{eff}$  is higher for the small grain sample than for the large grain sample. A fast-growing protective  $\text{Cr}_2\text{O}_3$  layer can be formed on the entire surface of the small grain sample due to the rapid diffusion of Cr along the grain boundaries. The rapid growth of  $\text{Cr}_2\text{O}_3$  in the small grain sample is also revealed by the results of the oxidation kinetics shown in Fig. 9 and Table 3.

#### 4.2.2. Critical grain size

As shown in this study, the presence of grain boundaries and the grain size are important factors to be considered to understand the formation of oxide layers. The spacing among the  $\text{Cr}_2\text{O}_3$  oxide regions formed on the grain boundaries decreases as the grain size of the austenitic stainless steel containing alloyed Cu is reduced. Therefore, less time is required for the sideward growth of the oxide nuclei to finally form a continuous protective  $\text{Cr}_2\text{O}_3$  layer based on the literature data for the Cr diffusion coefficient in the bulk and along the grain boundaries of a Fe–17–18 wt.% Cr–10–12 wt.% Ni steel [79,80] and in combination with the equations developed by Lobb and Evans [35]:

$$j_{GB}/j_L = \frac{2\delta}{d}(D_{GB}/D_L)^{1/2} \quad (3)$$

where  $j_{GB}/j_L$  is the flux ratio,  $\delta$  is the width of the grain boundary region,  $d$  is the grain size, and  $D_{GB}$  and  $D_L$  are the grain boundary and bulk diffusion coefficients, respectively.

Fig. 14 reveals that according to the decrease in grain size, the amount of Cr flux is increased due to the increase in the total grain boundary density. More than a 20% additional flux of Cr ions is supplied from the grain boundaries to the surface if the distance from the grain boundary is less than 4.5  $\mu\text{m}$ , and the amount of the flux increases drastically if it approaches the grain boundary. Thus, in the small grain sample, due to the grain boundaries, the Cr

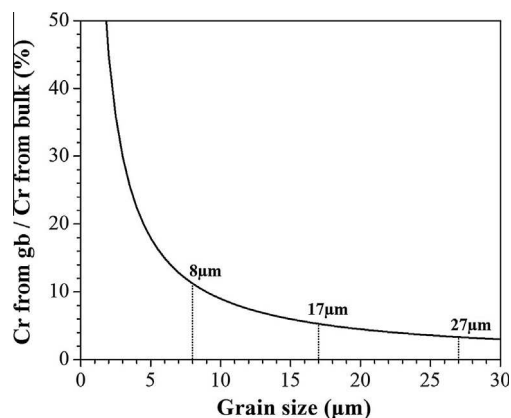


Fig. 14. Relative increase in the Cr flux via grain boundary diffusion as a function of grain size in Fe–18Cr–10Ni at 700 °C. The grain boundary width ( $\delta$ ) is 0.5 nm.

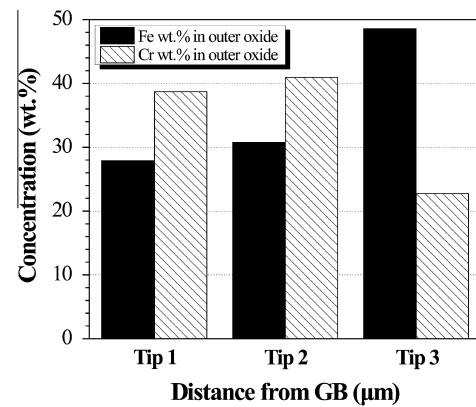


Fig. 15. Chemical composition (wt.%) of Fe (black solid bar) and Cr (white stripe bar) in the entire outer oxide of all tips as measured using APT.

diffusion to the surface region is enhanced, and sideward spreading of the external  $\text{Cr}_2\text{O}_3$  layer from the grain boundaries toward the grain interiors occurs, which enables the formation of a continuous protective  $\text{Cr}_2\text{O}_3$  layer over the entire sample surface. In the case of the austenitic stainless steel containing alloyed Cu, even 18 wt.% Cr is not always sufficient to form a protective  $\text{Cr}_2\text{O}_3$  oxide layer covering the entire surface. Instead, the growth of non-protective Fe-oxide leads to the observed mass gain. Fig. 15 reveals that the Cr wt.% in the outer oxide is strongly influenced by the distance from the grain boundary. The Cr concentration of the outer oxide close to the grain boundaries has approximately 40 wt.% Cr with a Fe concentration of 30 wt.%. The optimum Cr concentration range is between 23 and 40 wt.% for the maintenance of oxide adhesion and the formation of a protective  $\text{Cr}_2\text{O}_3$  on Fe–Cr alloys [81] at high temperatures. Near the grain boundary, the supply of Cr via both grain boundary and bulk diffusion is sufficient to form a protective  $\text{Cr}_2\text{O}_3$  oxide layer; however, in the intra-grain regions far from the grain boundary, the supply of Cr is primarily provided by bulk diffusion, which cannot maintain a sufficiently high Cr concentration to form a protective  $\text{Cr}_2\text{O}_3$  oxide. In this region, the outer oxide is produced from a protective Cr-rich oxide to a non-protective Fe-rich oxide, such as  $\text{Fe}_3\text{O}_4$  and  $\text{Fe}_2\text{O}_3$ . This oxide phase transition illustrates the selective oxidation behavior of these austenitic stainless steels containing alloyed Cu. In particular, the formation of  $\text{Cr}_2\text{O}_3$  is enabled when the distance from a grain boundary is smaller than 4  $\mu\text{m}$  (i.e., for samples with a grain size below 8  $\mu\text{m}$ ). The calculated grain size and concentration values of Cr to form the protective  $\text{Cr}_2\text{O}_3$  layer are in reasonable agreement with the experimental data obtained in this study. Finally, the protective  $\text{Cr}_2\text{O}_3$  layer at the oxide/matrix interface acts as an effective diffusion barrier against the further transport of oxygen and metal ions. Further investigation into the stability of this protective layer for longer oxidation periods (up to 500 h) is available in a previous study by the authors [41].

## 5. Conclusions

The high-temperature oxidation behavior of an austenitic stainless steel containing alloyed Cu has been studied with respect to the role of the grain boundaries and the resulting critical grain size to form a uniform protective  $\text{Cr}_2\text{O}_3$  oxide. The following conclusions can be drawn:

- (1) Selective retarded oxidation is observed within a certain distance from random grain boundaries toward the grain interiors.  $\Sigma 3$  CSL grain boundaries do not contribute to this selective oxidation. Thus, the oxidation rate depends on the grain size neglecting  $\Sigma 3$  boundaries.

- (2) During the initial stage (~30 min) of oxidation, the outer oxide layers formed <4 μm away from random grain boundaries and are mainly composed of protective Cr<sub>2</sub>O<sub>3</sub> with a rhombohedral crystal structure and thin Fe-rich (Fe,Cr)<sub>3</sub>O<sub>4</sub>. In contrast, if the outer oxide layer formed >4 μm away from random grain boundaries, it consists of a thick Fe-rich (Fe,Cr)<sub>3</sub>O<sub>4</sub> oxide with a spinel crystal structure containing small amounts of Ni, Mn and Cu, whereas the inner layer mainly consists of Cr-rich (Fe,Cr)<sub>3</sub>O<sub>4</sub> oxides with spinel crystal structures.
- (3) In the later stage (~2 h) of oxidation, the samples with large grain sizes (>8 μm) form a duplex oxide. A thick Fe-rich oxide is formed in the intra-grain regions, whereas a thinner Cr-rich oxide is formed at the grain boundaries. These results are in contrast with the measurements of samples with a small grain size (<8 μm). For those samples, a uniform protective Cr-rich oxide is formed. As a result, the overall oxidation of small-grained sample can be suppressed.

The present study shows that grain size refinement (with a critical grain size of 8 μm) is an advantageous approach to increase the resistance to high-temperature oxidation under humid air conditions without increasing the Cr content or adding additional elements.

### Acknowledgements

This work was supported by KIST (Grant Number 2E25322). Mr. Ju-Heon Kim's stay at the Max-Planck Institut für Eisenforschung (MPIE) was supported by the MPIE scholarship and the Deutscher Akademischer Austausch Dienst (DAAD) scholarship for doctoral candidates and young academics and scientists.

### References

- [1] R. Viswanathan, W. Bakker, Materials for ultrasupercritical coal power plants – boiler materials: Part 1, *J. Mater. Eng. Perform.* 10 (2001) 81–95.
- [2] R. Viswanathan, J. Sarver, J.M. Tanzosh, Boiler materials for ultra-supercritical coal power plants – steamside oxidation, *J. Mater. Eng. Perform.* 15 (2006) 255–274.
- [3] C.A. Powell, B.D. Morreale, Materials challenges in advanced coal conversion technologies, *MRS Bull.* 33 (2008) 309–315.
- [4] A. Zieliński, Austenitic steels for boiler elements in USC power plants, *JAMME* 57 (2013) 68–75.
- [5] C. Chi, H. Yu, X. Xie, Advanced austenitic heat-resistant steels for Ultra-Super-Critical (USC) fossil power plants, in alloy steel – properties and use, *InTech* (2011) 171–200.
- [6] C. Chi, H. Yu, J. Dong, X. Xie, Z. Cui, X. Chen, F. Lin, Strengthening effect of Cu-rich phase precipitation in 18Cr9Ni3CuNbN austenitic heat-resisting steel, *Acta Metall. Sin. (English Letters)* 24 (2011) 141–147.
- [7] C. Cheng-Yu, Y. Hong-Yao, D. Jian-Xin, L. Wen-Qing, C. Shi-Chang, L. Zheng-Dong, X. Xi-Shan, The precipitation strengthening behavior of Cu-rich phase in Nb contained advanced Fe–Cr–Ni type austenitic heat resistant steel for USC power plant application, *Prog. Nat. Sci.: Mater. Int.* 22 (2012) 175–185.
- [8] B.M. Gonzalez, C.S.B. Castro, V.T.L. Buono, J.M.C. Vilela, M.S. Andrade, J.M.D. Moraes, M.J. Mantel, The influence of copper addition on the formability of AISI 304 stainless steel, *Mater. Sci. Eng. A* 343 (2003) 51–56.
- [9] Y. Sawaragi, S. Hirano, The development of a new 18–8 austenitic steel (0.1C–18Cr–9Ni–3Cu–Nb, N) with high elevated temperature strength for fossil fired boilers, *Mech. Beh. M.* 4 (1992) 589–594.
- [10] Y. Sawaragi, N. Otsuka, H. Senba, S. Yamamoto, Properties of a new 18–8 austenitic steel tube (SUPER 304H) for fossil fired boilers after service exposure with high elevated temperature strength, *Sumitomo Search* 56 (1994) 34–43.
- [11] F. Riffard, H. Buscail, E. Caudron, R. Cueff, C. Issartel, S. El Messki, S. Perrier, A new interpretation of the “breakaway” oxidation behaviour observed at high temperature on 304 stainless steel, *Mater. Sci. Forum.* 461–464 (2004) 175–182.
- [12] X. Peng, J. Yan, Y. Zhou, F. Wang, Effect of grain refinement on the resistance of 304 stainless steel to breakaway oxidation in wet air, *Acta Mater.* 53 (2005) 5079–5088.
- [13] S. Cissé, L. Laffont, B. Tanguy, M.-C. Lafont, E. Andrieu, Effect of surface preparation on the corrosion of austenitic stainless steel 304L in high temperature steam and simulated PWR primary water, *Corros. Sci.* 56 (2012) 209–216.
- [14] F. Riffard, H. Buscail, E. Caudron, R. Cueff, C. Issartel, S. Perrier, Effect of yttrium addition by sol–gel coating and ion implantation on the high temperature oxidation behaviour of the 304 steel, *Appl. Surf. Sci.* 199 (2002) 107–122.
- [15] F.J. Pérez, M.J. Cristóbal, M.P. Hierro, F. Pedraza, G. Arnau, T.P. Merino, Effect of yttrium and erbium ion implantation on the oxidation behaviour of the AISI 304 austenitic steel, *Surf. Coat. Technol.* 126 (2000) 116–122.
- [16] F.J. Pérez, E. Otero, M.P. Hierro, C. Gómez, F. Pedraza, J.L. de Segovia, E. Román, High temperature corrosion protection of austenitic AISI 304 stainless steel by Si, Mo and Ce ion implantation, *Surf. Coat. Technol.* 108–109 (1998) 127–131.
- [17] C. Issartel, Nitridation effect on the oxidation of a austenitic stainless steel AISI 304 at 900 °C, *Appl. Surf. Sci.* 225 (2004) 14–20.
- [18] M.D. Merz, The oxidation resistance of fine-grained sputter-deposited 304 stainless steel, *Metall. Trans. A* 10 (1979) 71–77.
- [19] T. Tanabe, S. Imoto, Surface oxidation of type 316 stainless steel, *Trans. Jpn. Inst. Met.* 20 (1979) 507–515.
- [20] M.J. Capitán, A. Paúl, J.L. Pastol, J.A. Odriozola, X-ray diffraction study of oxide scales formed at high temperatures on AISI 304 stainless steel after cerium deposition, *Oxid. Met.* 52 (1999) 447–462.
- [21] G. Betz, G.K. Wehner, L. Toth, A. Joshi, Composition-vs-depth profiles obtained with auger electron spectroscopy of air-oxidized stainless-steel surfaces, *Jpn. J. Appl. Phys.* 45 (1974) 5312–5316.
- [22] L. Dong-Sheng, D. Qi-Xun, C. Xiao-Nong, W. Rong-Rong, H. Yan, High-temperature oxidation resistance of austenitic stainless steel Cr18Ni11Cu3Al3MnNb, *J. Iron Steel. Res. Int.* 19 (2012) 74–78.
- [23] E.A. Gulbransen, K.F. Andrew, Oxidation studies on 304 stainless steel, *J. Electrochem. Soc.* 109 (1962) 560–564.
- [24] H. Asteman, J.E. Svensson, M. Norell, L.G. Johansson, Influence of water vapor and flow rate on the high-temperature oxidation of 304L; effect of chromium oxide hydroxide evaporation, *Oxid. Met.* 54 (2000) 11–26.
- [25] H. Asteman, J.E. Svensson, L.G. Johansson, Oxidation of 310 steel in H<sub>2</sub>O/O<sub>2</sub> mixtures at 600 °C: the effect of water-vapour-enhanced chromium evaporation, *Corros. Sci.* 44 (2002) 2635–2649.
- [26] G.C. Allen, J.M. Dyke, S.J. Harris, A. Morris, A surface study of the oxidation of type 304L stainless steel at 600 K in air, *Oxid. Met.* 29 (1988) 391–408.
- [27] D.R. Baer, Protective and non-protective oxide formation on 304 stainless steel, *Appl. Surf. Sci.* 7 (1981) 69–82.
- [28] D.P. Whittle, J. Stringer, Improvements in high temperature oxidation resistance by additions of reactive elements or oxide dispersions, *Math. Phys. Sci. A* 295 (1980) 309–329.
- [29] G. Yurek, D. Eisen, A. Garratt-Reed, Oxidation behavior of a fine-grained rapidly solidified 18–8 stainless steel, *Metall. Mater. Trans. A* 13 (1982) 473–485.
- [30] F.H. Stott, G.C. Wood, J. Stringer, The influence of alloying elements on the development and maintenance of protective scales, *Oxid. Met.* 44 (1995) 113–145.
- [31] N. Karimi, F. Riffard, F. Rabaste, S. Perrier, R. Cueff, C. Issartel, H. Buscail, Characterization of the oxides formed at 1000 °C on the AISI 304 stainless steel by X-ray diffraction and infrared spectroscopy, *Appl. Surf. Sci.* 254 (2008) 2292–2299.
- [32] S.E. Ziemniak, M. Hanson, Corrosion behavior of 304 stainless steel in high temperature, hydrogenated water, *Corros. Sci.* 44 (2002) 2209–2230.
- [33] A.M. Huntz, A. Reckmann, C. Haut, C. Sévéc, M. Herbst, F.C.T. Resende, A.C.S. Sabioni, Oxidation of AISI 304 and AISI 439 stainless steels, *Mater. Sci. Eng. A* 447 (2007) 266–276.
- [34] H.E. Evans, D.A. Hilton, R.A. Holm, Chromium-depleted zones and the oxidation process in stainless steels, *Oxid. Met.* 10 (1976) 149–161.
- [35] R.C. Lobb, H.E. Evans, Formation of protective oxide film on chromium-depleted stainless steel, *Met. Sci.* 15 (1981) 267–274.
- [36] R. Davis, *Stainless steels*, ASM Speciality Handbook, ASM, Materials Park, 1994.
- [37] I.G. Wright, B.A. Pint, ORNL, *Corrosion*, 2002 (Denver, 2002).
- [38] G.C. Wood, The oxidation of iron-chromium alloys and stainless steels at high temperatures, *Corros. Sci.* 2 (1962) 173–196.
- [39] D. Baer, M. Merz, Differences in oxides on large-and small-grained 304 stainless steel, *Metall. Mater. Trans. A* 11 (1980) 1973–1980.
- [40] S.N. Basu, G.J. Yurek, Effect of alloy grain size and silicon content on the oxidation of austenitic Fe–Cr–Ni–Mn–Si alloys in pure O<sub>2</sub>, *Oxid. Met.* 36 (1991) 281–315.
- [41] J.-H. Kim, D.-I. Kim, S. Suwas, E. Fleury, K.-W. Yi, Grain-size effects on the high-temperature oxidation of modified 304 austenitic stainless steel, *Oxid. Met.* 79 (2013) 239–247.
- [42] S.G. Wang, M. Sun, H.B. Han, K. Long, Z.D. Zhang, The high-temperature oxidation of bulk nanocrystalline 304 stainless steel in air, *Corros. Sci.* 72 (2013) 64–72.
- [43] T. Terachi, T. Yamada, T. Miyamoto, K. Arioka, K. Fukuya, Corrosion behavior of stainless steels in simulated PWR primary water – effect of chromium content in alloys and dissolved hydrogen, *J. Nucl. Sci. Technol.* 45 (2008) 975–984.
- [44] K. Kruska, S. Lozano-Perez, D.W. Saxey, T. Terachi, T. Yamada, G.D.W. Smith, Nanoscale characterisation of grain boundary oxidation in cold-worked stainless steel, *Corros. Sci.* 63 (2012) 225–233.
- [45] C. Oberdorfer, P. Stender, C. Reinke, G. Schmitz, Laser-assisted atom probe tomography of oxide materials, *Microsc. Microanal.* 13 (2007) 342–346.
- [46] S. Lozano-Perez, D.W. Saxey, T. Yamada, T. Terachi, Atom-probe tomography characterization of the oxidation of stainless steel, *Scripta Mater.* 62 (2010) 855–858.
- [47] K. Thompson, D. Lawrence, D.J. Larson, J.D. Olson, T.F. Kelly, B. Gorman, In situ site-specific specimen preparation for atom probe tomography, *Ultramicroscopy* 107 (2007) 131–139.

- [48] J. Takahashi, K. Kawakami, Y. Yamaguchi, M. Sugiyama, Development of atom probe specimen preparation techniques for specific regions in steel materials, *Ultramicroscopy* 107 (2007) 744–749.
- [49] M.K. Miller, K.F. Russell, Atom probe specimen preparation with a dual beam SEM/FIB miller, *Ultramicroscopy* 107 (2007) 761–766.
- [50] M.P. Phaniraj, D.-I. Kim, Y.W. Cho, Effect of grain boundary characteristics on the oxidation behavior of ferritic stainless steel, *Corros. Sci.* 53 (2011) 4124–4130.
- [51] D.-I. Kim, S.H. Hong, M.P. Phaniraj, H.N. Han, J.-P. Ahn, Y.W. Cho, Microstructural analysis of oxide layer formation in ferritic stainless steel interconnects, *Mater. High Temp.* 28 (2011) 285–289.
- [52] B. Chattopadhyay, G.C. Wood, The transient oxidation of Fe–Cr and Ni–Cr alloys, *J. Electrochem. Soc.* 117 (1970) 1163–1171.
- [53] M.G.C. Cox, B. McEnaney, V.D. Scott, Vacancy condensation and void formation in duplex oxide scales on alloys, *Philos. Mag.* 28 (1973) 309–319.
- [54] C. Desgranges, F. Lequien, E. Aublant, M. Nastar, D. Monceau, Depletion and voids formation in the substrate during high temperature oxidation of Ni–Cr alloys, *Oxid. Met.* 79 (2013) 93–105.
- [55] Y. Gong, B. Cooman, Kirkendall void formation during selective oxidation, *Metall. Mater. Trans. A* 41 (2010) 2180–2183.
- [56] N. Otsuka, Y. Shida, H. Fujikawa, Internal–external transition for the oxidation of Fe–Cr–Ni austenitic stainless steels in steam, *Oxid. Met.* 32 (1989) 13–45.
- [57] C. Chi, J. Dong, W. Liu, X. Xie, 3DAP investigation of precipitation behavior of Cu-rich phase in Super304H heat resistant steel, *Jinshu Xuebao/Acta Metall. Sin.* 46 (2010) 1141–1146.
- [58] J.-H. Kim, D.-I. Kim, J.-H. Shim, K.-W. Yi, Investigation into the high temperature oxidation of Cu-bearing austenitic stainless steel using simultaneous electron backscatter diffraction-energy dispersive spectroscopy analysis, *Corros. Sci.* 77 (2013) 397–402.
- [59] J.-H. Kim, D.-I. Kim, P.-P. Choi, D. Raabe, K.-W. Yi, in preparation.
- [60] N.K. Das, K. Suzuki, K. Ogawa, T. Shoji, Early stage SCC initiation analysis of fcc Fe–Cr–Ni ternary alloy at 288 °C: a quantum chemical molecular dynamics approach, *Corros. Sci.* 51 (2009) 908–913.
- [61] T. Terachi, K. Fujii, K. Arioka, Microstructural characterization of SCC crack tip and oxide film for SUS 316 stainless steel in simulated PWR primary water at 320 °C, *J. Nucl. Sci. Technol.* 42 (2005) 225–232.
- [62] C. Wagner, *Atom Movements*, ASM, Cleveland, 1951.
- [63] B. Pieraggi, Calculations of parabolic reaction rate constants, *Oxid. Met.* 27 (1987) 177–185.
- [64] C. Wagner, *J. Phys. Chem. B* 21 (1933) 25.
- [65] A.F. Smith, The oxidation of an 18/8 type stainless steel in CO<sub>2</sub>, *Mater. Corros.* 30 (1979) 100–104.
- [66] G. Wood, High-temperature oxidation of alloys, *Oxid. Met.* 2 (1970) 11–57.
- [67] S.J. Rothman, L.J. Nowicki, G.E. Murch, Self-diffusion in austenitic Fe–Cr–Ni alloys, *J. Phys. F. Met. Phys.* 10 (1980) 383.
- [68] D. Caplan, P.E. Beaubien, M. Cohen, Effect of manganese on the high-temperature oxidation of Fe–26Cr alloy, *Trans. Met. Soc.* 233 (1965) 766.
- [69] F.H. Stott, F.I. Wei, C.A. Enahoro, The influence of manganese on the high-temperature oxidation of iron–chromium alloys, *Mater. Corros.* 40 (1989) 198–205.
- [70] K. Ledjef, A. Rahmel, M. Schorr, Oxidation and carburization of high alloyed materials for cracking tubes Part 1: The oxidation behaviour in air, *Mater. Corros.* 30 (1979) 767–784.
- [71] P. Kofstad, K.P. Lillerud, On high temperature oxidation of chromium: II. Properties of Cr<sub>2</sub>O<sub>3</sub> and the oxidation mechanism of chromium, *J. Electrochem. Soc.* 127 (1980) 2410–2419.
- [72] R.E. Lobnig, H.P. Schmidt, K. Hennesen, H.J. Grabke, Diffusion of cations in chromia layers grown on iron-base alloys, *Oxid. Met.* 37 (1992) 81–93.
- [73] F.H. Stott, Influence of alloy additions on oxidation, *Mater. Sci. Technol.* 5 (1989) 734–740.
- [74] A.F. Smith, The oxidation of 18/8 type stainless steel in high pressure CO<sub>2</sub>/2% CO, *Mater. Corros.* 32 (1981) 1–7.
- [75] J. Ehlers, D.J. Young, E.J. Smaardijk, A.K. Tyagi, H.J. Penkalla, L. Singheiser, W.J. Quadackers, Enhanced oxidation of the 9%Cr steel P91 in water vapour containing environments, *Corros. Sci.* 48 (2006) 3428–3454.
- [76] E.W. Hart, On the role of dislocations in bulk diffusion, *Acta Metall. Mater.* 5 (1957) 597.
- [77] A. Atkinson, Diffusion along grain boundaries and dislocations in oxides, alkali halides and carbides, *Solid State Ionics* 12 (1984) 309–320.
- [78] B. Fultz, H.N. Frase, Grain boundaries of nanocrystalline materials – their widths, compositions, and internal structures, *Hyperfine Interact.* 130 (2000) 81–108.
- [79] R.A. Perkins, R.A. Padgett, N.K. Tunali, Tracer diffusion of 59Fe and 51Cr in Fe–17 Wt Pet Cr–12 Wt Pet Ni austenitic alloy, *Metall. Trans.* 4 (1973) 2535–2540.
- [80] I. Kaur, W. Gust, *Fundamentals of Grain and Interface Boundary Diffusion*, second revised ed., Ziegler Press, Stuttgart, 1989.
- [81] D.P. Whittle, G.C. Wood, Chromium oxide scale growth on iron–chromium alloys: II. Influence of alloy composition, *J. Electrochem. Soc.* 115 (1968) 133–142.
- [82] E. Opila, N. Jacobson, D. Myers, E. Copland, Predicting oxide stability in high-temperature water vapor, *JOM* 58 (2006) 22–28.